

STUDY ON MEASUREMENT OF RESIDUAL STRESSES IN DED BASED ADDITIVELY MANUFACTURED SS316L COMPONENTS

*A thesis report submitted in partial fulfilment of the
requirements for the degree of*

MASTER OF TECHNOLOGY

by

DIGVIJAY CHANDRASEN THAKARE

Roll No: 234103415

Under the supervision of

Dr. SRIKRISHNA N. JOSHI



**DEPARTMENT OF MECHANICAL ENGINEERING
INDIAN INSTITUTE OF TECHNOLOGY GUWAHATI
GUWAHATI- 781039, INDIA**

May, 2025

STUDY ON MEASUREMENT OF RESIDUAL STRESSES IN DED BASED ADDITIVELY MANUFACTURED SS316L COMPONENTS

*A thesis report submitted in partial fulfilment of the
requirements for the degree of*

MASTER OF TECHNOLOGY

by

DIGVIJAY CHANDRASEN THAKARE

Roll No: 234103415

Under the supervision of

Dr. SRIKRISHNA N. JOSHI



**DEPARTMENT OF MECHANICAL ENGINEERING
INDIAN INSTITUTE OF TECHNOLOGY GUWAHATI
GUWAHATI- 781039, INDIA**

May, 2025



**Department of Mechanical Engineering
Indian Institute of Technology Guwahati
Guwahati, Assam, India-781039**

CERTIFICATE

This is to certify that the work contained in this thesis titled “**STUDY ON MEASUREMENT OF RESIDUAL STRESSES IN DED BASED ADDITIVELY MANUFACTURED SS316L COMPONENTS**” by **Mr. DIGVIJAY CHANDRAASEN THAKARE (234103415)**, a student of the Department of Mechanical Engineering, Indian Institute of Technology Guwahati, for the award of degree of **Master of Technology** has been carried out under my supervision and that this work has not been submitted elsewhere for any degree.

Dr. Shrikrishna N. Joshi

Professor

Department of Mechanical Engineering
Indian Institute of Technology Guwahati
Guwahati, Assam, India – 781039

May 2025

DECLARATION

I declare that this written submission represents my ideas in my own words and where others' ideas or words have been included, I have adequately cited and referenced the sources. I also declare that I have adhered to all principles of academic honesty and integrity and have not misrepresented or fabricated or falsified any idea or data or fact or source in my submission. I understand that any violation of the above will be cause for disciplinary action by the Institute and can also evoke penal action from the sources that have thus not been properly cited or from whom proper permission has not been taken when needed.

Mr. Digvijay Chandrasen Thakare (234103415)

Machine Design (2023-25)

Department of Mechanical Engineering

Indian Institute of Technology Guwahati

Guwahati, Assam, India – 781039

May 2025

ACKNOWLEDGEMENT

Firstly, I would like to express my sincere gratitude and appreciation to my supervisor, Dr. Shrikrishna N. Joshi, Professor, Department of Mechanical Engineering, IIT Guwahati, India, for their unwavering guidance, expertise, and continuous encouragement throughout the course of this research. His mentorship has been instrumental in shaping and helped me to complete this work successfully. I am indebted to the dedicated staff at Department of Mechanical Engineering, IIT Guwahati, India, who provided technical assistance, insightful discussions, and shared their expertise, which significantly contributed to the success of this project.

I am especially grateful to Mrs. Varsharani Y. Gaikhe, Mr. Antash Sinha, Mr. Niranjan Padwale, Mr. Udit Kumar for their help in the experimentation of the project.

The scholarship received from MHRD (Ministry of Human Resource Development), Government of India, during my M.Tech. is gratefully acknowledged. Finally, I sincerely thank my family for their constant support throughout my master's program. I also appreciate everyone who has inspired and motivated me during this journey. Their encouragement and faith in me have played a significant role in keeping me focused. This work would not have been accomplished without the combined support and efforts of these individuals and organizations. I am genuinely grateful for their contributions to my academic and research pursuits.

Mr. Digvijay Chandrasen Thakare (234103415)

Machine Design (2023-25)

Department of Mechanical Engineering

Indian Institute of Technology Guwahati

Guwahati, Assam, India – 781039

May 2025

ABSTRACT

This study investigates the microstructural and mechanical characteristics of 316L stainless steel fabricated using the Laser Wire Directed Energy Deposition (LWDED) process. The work aims to evaluate the suitability of LWDED for producing high-integrity components through detailed characterisation. Microhardness testing was conducted to assess the variation in hardness across the deposited layers. Field Emission Scanning Electron Microscopy (FESEM) was employed to analyse the surface morphology, grain structure, and possible defects formed during the deposition process. X-ray Diffraction (XRD) analysis was performed to quantify residual stresses induced by the thermal cycles inherent to LWDED. The findings provide insights into the influence of thermal gradients on microstructural evolution and residual stress development, contributing to a better understanding of the LWDED process for 316L stainless steel and its potential for metal additive manufacturing applications requiring high strength and corrosion resistance.

Table of Content

CERTIFICATE.....	i
DECLARATION.....	ii
ACKNOWLEDGEMENT	iii
ABSTRACT.....	iv
Table of Content.....	v
Abbreviation.....	vii
List of Figures	viii
List of Tables.....	xi
INTRODUCTION	1
1.1 Additive Manufacturing Technology Process.....	1
1.1.1 Powder Bed Fusion (PBF)	3
1.1.2 Directed Energy Deposition (DED).....	3
1.1.3 Material Extrusion	4
1.1.4 Vat Polymerisation.....	4
1.1.5 Binder Jetting	5
1.1.6 Material Jetting	5
1.1.7 Sheet Lamination Process	6
1.2 Metal Additive Manufacturing.....	6
1.3 Laser Wire Direct Energy Deposition.....	6
1.3.1 Material used for AM: SS 316L.....	8
1.4 Residual Stresses in AM	8
1.5 XRD for Measurement of Residual Stress.....	9
LITERATURE REVIEW	11
2.1 Metal Additive Manufacturing.....	11
2.2 Laser Wire Direct Energy Deposition.....	11
2.3 Stainless Steel 316L in AM.....	13
2.4 Heat Source Model	14
2.5 Residual Stress.....	15
2.5.1 Bragg's Law	16
2.5.2 Diffractometer Geometry	18
2.5.3 Strain Measurement	20
2.5.4 Stress Determination.....	22
2.5.5 $\sin^2 \Psi$ Method.....	22

2.6	Objectives of the Study	23
METHODOLOGY		24
3.1	Numerical Analysis	24
3.2	Sample Fabrication	25
3.3	Microhardness	29
3.4	X-Ray Diffraction (XRD) for Residual Stress	31
3.5	Field Emission Scanning Electron Microscopy (FESEM)	32
RESULTS and DISCUSSION		33
4.1	Visual and Dimensional Inspection	33
4.2	COMSOL Simulation	34
4.3	Microhardness Analysis	35
4.4	Analysis under FESEM.....	37
4.5	XRD Results and Analysis.....	38
4.5.1	Residual Stress in Top sample	41
4.5.2	Residual Stress in Middle sample	43
4.5.3	Residual Stress in Bottom sample.....	45
CONCLUSION		47
REFERENCES.....		50

Abbreviation

3D	Three Dimensional
AM	Additive Manufacturing
ASTM	American Society for Testing and Materials
CAD	Computer Aided Designing
CNC	Computer Numerical Control
DED	Direct Energy Disposition
EDM	Electrical Discharge Machining
FESEM	Field Emission Scanning Electron Microscope
HVN	Hardness Vicker Number
ISO	International Organization for Standardization
LWDED	Laser Wire Direct Energy Deposition
MAM	Metal Additive Manufacturing
RP	Rapid Printing
SLM	Selective Laser Melting
SLS	Selective Laser Sintering
SS	Stainless Steel
WAAM	Wire Arc Additive Manufacturing
XRD	X-Ray Diffraction

List of Figures

Figure 1: Powder Bed Fusion	3
Figure 2: Direct Energy Deposition	3
Figure 3: Material Extrusion	4
Figure 4: Vat Polymerisation	4
Figure 5: Binder Jetting	5
Figure 6: Material Jetting	5
Figure 7: Schematic Diagram of LWDED	7
Figure 8: Classification and measurement method of residual stress	9
Figure 9: Schematic Diagram of XRD	10
Figure 10: Goldak double ellipsoidal heat source	14
Figure 11: Gaussian heat source model	15
Figure 12: Diffraction of X-ray by a crystal	17
Figure 13: X-Ray diffractometer scheme	19
Figure 14: Focusing in the X-ray diffractometer	19
Figure 15: Co-ordinate system used for calculating surface strain and stresses	20
Figure 16: Schematic showing diffraction planes parallel to the surface and at an angle $\phi\psi$..	21
Figure 17: MELTIO M450	25
Figure 19: Additively Manufactured Part	27
Figure 20: (a)- Wire EDM Machine, (b)- Automatic Pneumatic mounting Press Machine	28
Figure 21: Moulded Sectioned Samples	29
Figure 22: Schematic of the Vickers Microhardness method test	30
Figure 23: XRD facility at IITG	31
Figure 24: Draft for Wire Cut EDM	33
Figure 25: COMSOL- Melt pool Simulation	34
Figure 26: Temperature profile	35
Figure 27: Vicker Microhardness Results	36
Figure 28: SEM Images of SS 316L	37
Figure 29: Diffractograms	38
Figure 30: XRD peaks of reference material	39
Figure 31: XRD peaks for Top sample, shifting of peak at 74.5°	41
Figure 32: d versus $\sin^2\psi$ linear fitted graph	42
Figure 33: XRD peaks for Middle sample, shifting of peak at 95.7°	43
Figure 34: d versus $\sin^2\psi$ linear fitted graph	44
Figure 35: XRD peaks for Top sample, shifting of peak at 90.45°	45
Figure 36: d versus $\sin^2\psi$ linear fitted graph	46

List of Tables

Table 1:AM Technology Process	2
Table 2: Chemical Composition of SS 316L	8
Table 3: Effect of LWDED Process prameters	13
Table 4: Technical Specifications of MELTIO 450	26
Table 5: Printing Parameters for 316L	27
Table 6: Vicker Microhardness Values.....	35
Table 7: d-value at $\psi=0$	40
Table 8: X-ray diffraction results for Top sample	41
Table 9: X-ray diffraction results for Middle sample	43
Table 10: X-ray diffraction results for Bottom sample	45

CHAPTER 1

INTRODUCTION

Additive Manufacturing, widely known as 3D printing has played an important role in the recent decades, in various sectors. According to the ISO/ASTM 52900 standard, Additive Manufacturing is defined as the “*process of joining materials to make parts from 3D model data, usually layer upon layer, as opposed to subtractive manufacturing and formative manufacturing methodologies*”[1]. Additive Manufacturing has caught the attention of various industries, hobbyist, individuals, etc. due to its simple principle but vast use. Unlike in traditional manufacturing, where unwanted material is removed from the workpiece, in AM the material is added layer by layer, where each individual layer is progressively added, builds parts by depositing material only where it is needed to shape and achieve the intricate 3D component. This method of manufacturing not only reduces the wastage during removal of unwanted material in subtractive manufacturing, but also gives an edge to create complex designs in a single process. AM includes a variety of processes that differ by the material to be used, energy source, feedstock form, and deposition method, etc. Initially AM was used to develop prototypes, which were used to visualise the final products, this process was known as rapid prototyping [2]. This process was beneficial as AM took very less time to set up and the associated man power and tooling cost was less as compared to the subtractive manufacturing. As this process came in the limelight, the AM technology saw a lot of advancement and was used beyond the prototyping to rapid tooling. The advanced work and research resulted in the use of AM in production of final products and moulds. Additive Manufacturing provides the flexibility to use a wide range of materials such as metals, polymers, composites, ceramics, etc. with good mechanical properties.

1.1 Additive Manufacturing Technology Process

The ASTM F42 Committee has characterized seven standard process types for AM. The technique utilized to accumulate material layers determines each variety [3]. The most widely used methods are Powder Bed Fusion (PBF), Directed Energy Deposition (DED), Binder Jetting, and Sheet Lamination.

Table 1:AM Technology Process

Sr. No.	Process types	Brief Description	Related Technology	Materials
1	Powder Bed Fusion	Areas of a powder bed are selectively fused by thermal energy.	Electron beam melting (EBM), selective laser sintering (SLS)	Metals, Polymer
2	Directed Energy Deposition	Materials are fused by focused heat energy, which melts the substance as it is deposited	Laser metal deposition (LMD)	Metals
3	Material Extrusion	A nozzle is used to selectively discharge the material.	Fused deposition modelling (FDM)	Polymers
4	Vat Photo polymerization	Light-activated polymerization selectively cures liquid photopolymer in a vat.	Stereo lithography (SLA), digital light processing (DLP)	Photopolymers
5	Binder Jetting	To combine powder materials, a liquid bonding agent is selectively deposited.	Powder bed and inkjet head (PBIH), plaster-based 3D printing (PP)	Polymers, Foundry Sand, Metals
6	Material Jetting	Build material droplets are deposited selectively.	Multi-jet modelling (MJM)	Polymers, Waxes
7	Sheet Lamination	An object is created by bonding sheets of material.	Laminated object manufacturing (LOM), ultrasonic consolidation (UC)	Paper, Metals

1.1.1 Powder Bed Fusion (PBF)

In PBF, fine powder is spread evenly on a buildup platform. A power source, either an electron beam or laser source is used to melt and fuse the material powder. The material powder is then again spread evenly all over. This process continues till final component is manufactured.

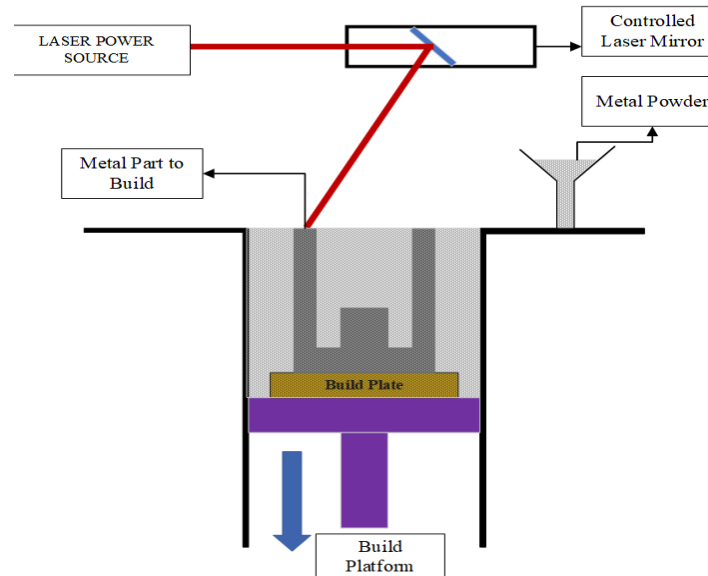


Figure 1: Powder Bed Fusion

1.1.2 Directed Energy Deposition (DED)

A metal additive manufacturing technique called Directed Energy Deposition (DED) is particularly useful for high-performance materials like superalloys [4]. Other names for it include Directed Light Fabrication (DLF), Direct Metal Deposition (DMD), etc. In DED, a nozzle is used to feed the material in powder or wire form, which is then melted using a heat source like electric arc or laser. The melted material is then deposited layer by layer.

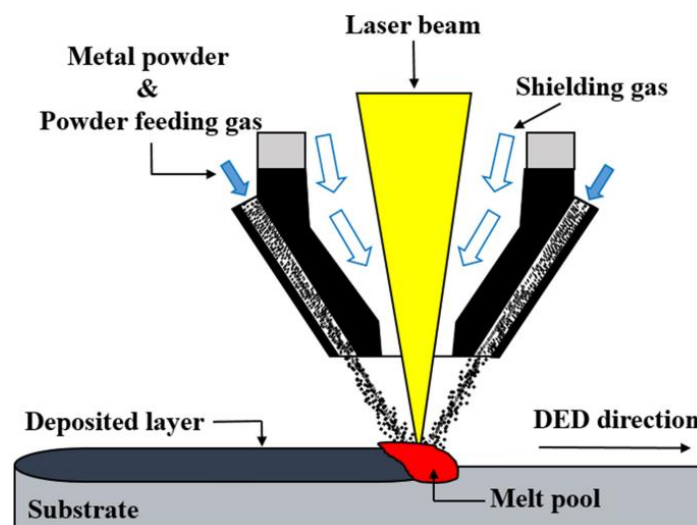


Figure 2: Direct Energy Deposition [5]

1.1.3 Material Extrusion

A popular material extrusion method called fused deposition modelling (FDM) involves drawing material through a nozzle, heating it, and then depositing it layer by layer. After every fresh layer is deposited, the platform travels up and down vertically and the nozzle can move horizontally. Chemical agents or temperature control can be used to bond layers of materials.

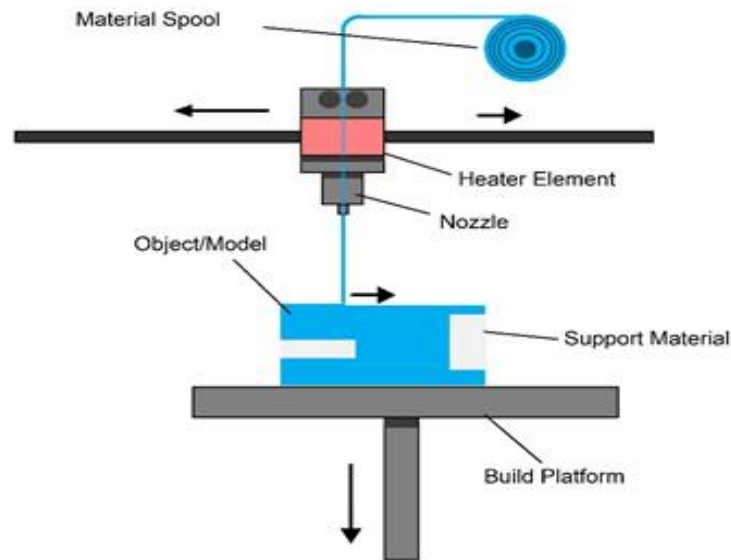


Figure 3: Material Extrusion [6]

1.1.4 Vat Polymerisation

The model is built layer by layer using a vat of liquid photopolymer resin, which is used in vat polymerization. Where necessary, an ultraviolet (UV) light is utilized to cure or harden the resin, and as each new layer is applied, a platform moves the object being created downward. There is no structural support from the material during the build phase because the method forms objects using liquid, as opposed to powder-based techniques, which rely on the unbound material for support. Support structures will frequently need to be added in this situation.

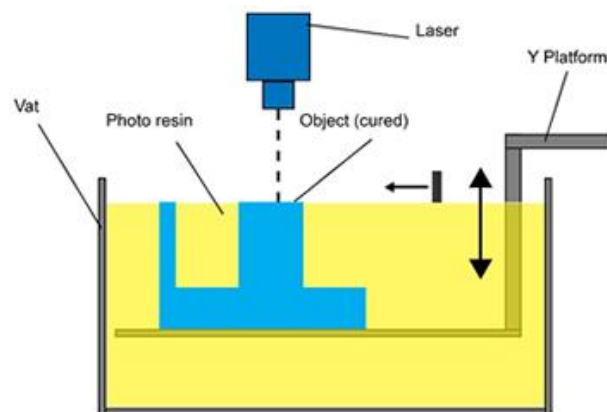


Figure 4: Vat Polymerisation [3]

1.1.5 Binder Jetting

Two ingredients are used in the binder jetting process: a binder and a powder-based substance. Between layers of powder, the binder serves as an adhesive. Typically, the construction material is in powder form and the binder is in liquid form. The build and binding materials are deposited in alternating layers by a print head that travels along the machine's horizontal axes. Despite the relative speed of printing, additional post-processing can add a significant amount of time to the whole process, and the material qualities are not always appropriate for structural elements due to the binding method.

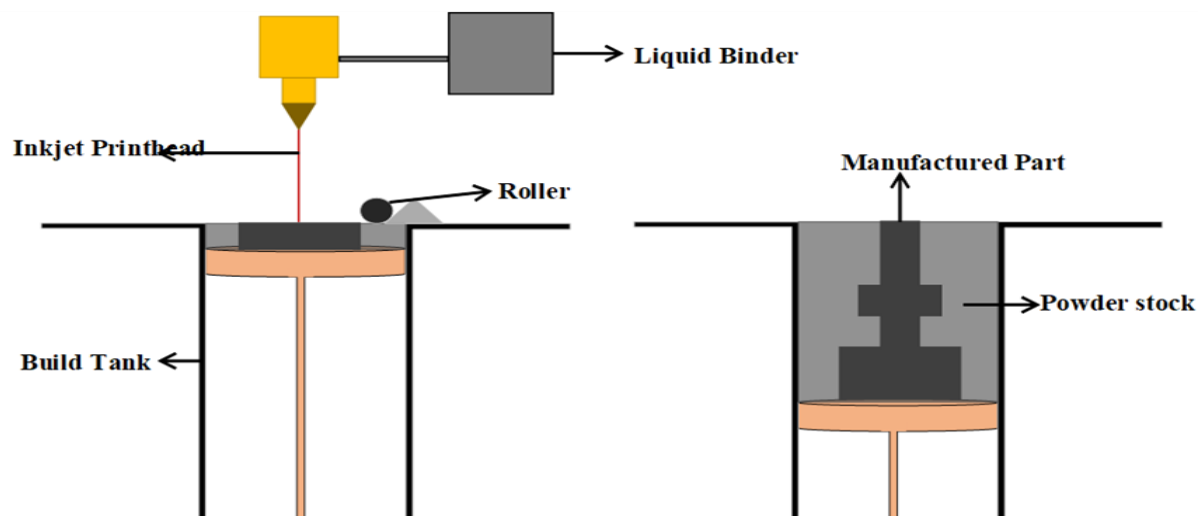


Figure 5: Binder Jetting [3]

1.1.6 Material Jetting

Material is continuously or Drop on Demand (DOD) shot onto a build platform, where it solidifies. The layers of material are then exposed to ultraviolet (UV) radiation to cure or harden them. Polymer and waxes are commonly used in this technique as the material is deposited drop by drop and viscous nature is required.

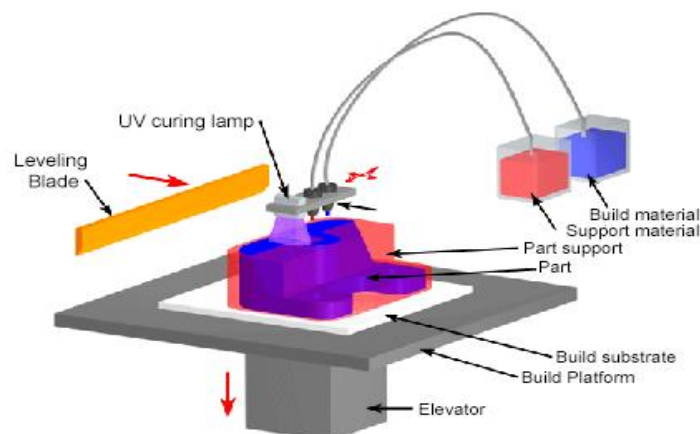


Figure 6: Material Jetting[3]

1.1.7 Sheet Lamination Process

Laminated object manufacturing (LOM) and ultrasonic additive manufacturing (UAM) are two methods of heat lamination. Metal sheets or ribbons used in the Ultrasonic Additive Manufacturing process are joined by ultrasonic welding. Additional CNC machining and the removal of the unbound metal during the welding process are necessary for this process. Similar layer-by-layer techniques are used in laminated object manufacturing (LOM), where paper and glue are used in place of welding. In order to facilitate the removal of post-build in the LOM process, the cross-hatching method is employed throughout the printing process.

1.2 Metal Additive Manufacturing

Metal Additive Manufacturing has gained significant attention due to its potential to produce high-strength, functional metal components with reduced lead times and material waste. Metal can be used in powder or wire form as per need and convenience[7]. The fundamental mechanism for the MAM is same for all different types of manufacturing techniques. The CAD model is uploaded in the brain of machine, which then uses a power source like a laser, electric arc, etc. to melt the powder or wire, which then gets deposited on the desired coordinates. The environment is such that the oxidation of molten metal is prevented at high temperatures [8]. The deposited metal is then solidified and bonds with the previous layer. Metal binder jetting, directed energy deposition, and powder bed fusion are the three main types of metal additive manufacturing techniques.

1.3 Laser Wire Direct Energy Deposition

A directed energy source, e.g., electric arc/plasma, laser beam, or electron beam, is used as an heat source in LWDED, to melt and join metal wire on a substrate in an effort to develop a 3D product layer by layer. Large deposition rates, mass production of components, strong and dense parts, near-net-shape deposition, and multiple metal handling capability is the forte of the DED technique. LWDED is best suited to use in surface coating, intricate part production, and repair due to its very good control over microstructure, geometry, and deposition rate. The method allows for transitions from different material compositions in a single component, and it is useful when fabricating functionally graded materials (FGMs). It is often used with metals

such as cobalt-chrome alloys, Inconel, titanium alloys, and stainless steels, particularly in tooling, aerospace, and biomedical industries.

Repairing and refurbishing expensive parts, including turbine blades, to increase their lifespan is one of LWDED's main advantages. Additionally, the procedure supports the production of shapes that are not achievable with conventional methods by enabling multi-axis deposition. But in order to increase the quality of the finished product, issues like thermal residual stress, porosity, and surface roughness frequently call for post-processing procedures like heat treatment and machining [9]. Due to its characteristics, which include high peak power, flexible pulse duration, good beam quality, and improved absorption in metals, CO₂ and Nd:YAG lasers [10] were previously extensively investigated in AM. However, these lasers frequently have some significant drawbacks. For example, CO₂ lasers cannot carry beams through optical fibre, and Nd:YAG lasers may only have a limited power output and be limited in their ability to operate in pulse mode. Currently, fibre lasers are the method of choice [11].

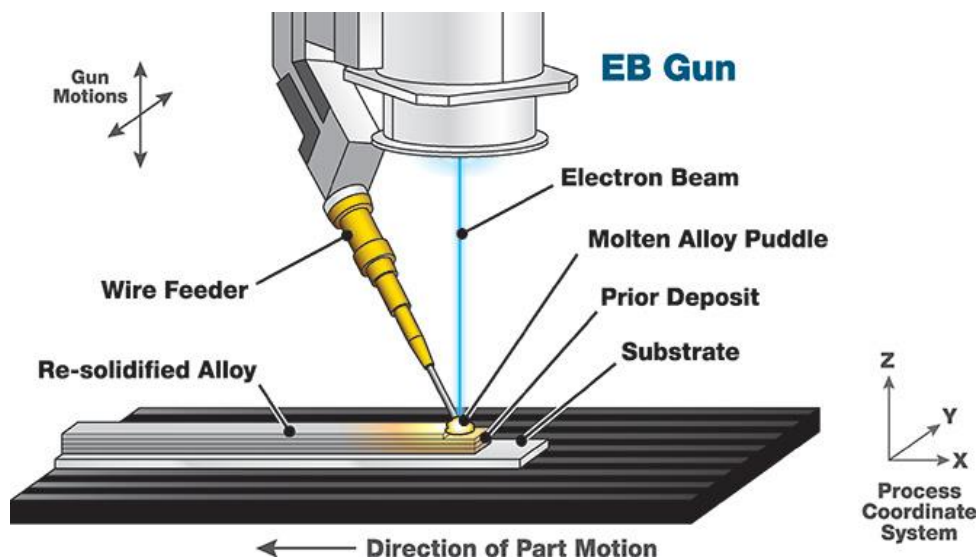


Figure 7: Schematic Diagram of LWDED [5]

A number of process parameters that affect the quality, shape, and characteristics of the deposited material have a major impact on LWDED performance. The parameters, which need to be carefully managed are laser power, scanning speed, wire feed rate, and shielding gas flow rate, etc. While scanning speed regulates the cooling rate and bead shape, laser power influences the size of the melt pool and penetration depth. The rate of material deposition and layer thickness are determined by the wire feed rate[12]. The LWDED process's large thermal gradients and quick thermal cycles can have a big impact on the material's mechanical and thermal behaviour during deposition. These circumstances frequently cause residual stresses to build within the constructed item, which may have an impact on its service performance,

structural integrity, and dimensional accuracy [13]. Apart from experimental works Researchers have analysed the laser wire process through numerical simulation for the prediction of melt pool dimensions thermal characterization

Knowledge of the thermal behaviour and heat transport during production requires thermal simulation of the LWDED. The laser generates temperature gradients in the deposited material due to which deformation, development of residual stress, and microstructural evolution take place. Temperature distribution, cooling rates, dynamics of the melt pool, etc. can be modelled with the help of numerical simulation [14]. Process parameters can be optimised, increase component quality, and minimize defects by accurately simulating the thermal history. Thermal simulation is one of the many such technique utilized in the work to relate temperature fields to the stress development in SS316L components produced with LWDED [15].

1.3.1 Material used for AM: SS 316L

The good mechanical strength, weldability, and corrosion resistance, stainless steel 316L has huge usage in AM. Due to these features, it is best suited for the LWDED process, which needs good metallurgical bonding and precise material control. Due to this, SS316L has found extensive application in the biomedical, aircraft, tooling, marine industries, etc where high-performance, corrosion-resistant parts are required. Although, microstructure and mechanical properties could be affected by the repeated heat cycling during deposition, leads to generation of residual stresses.

Table 2: Chemical Composition of SS 316L

Wire Chemical Composition	Fe	C	Si	Mn	Cr	Ni	Mo
Weight Percent [%]	Bal.	0.02	0.9	1.7	18.5	12.0	2.7

1.4 Residual Stresses in AM

Layer by layer, the solidified material gets deposited, with the help of a heat source. Strong, cyclic, and unstable heating and cooling are involved in this process, making the AM sample vulnerable to complicated thermal stress fields and thermal histories. Similar to welding, the part will have a significant residual stress due to this complex thermal stress field and thermal history. When a material is exposed to the radiation from a heat source and rapidly heated to the melting point, a molten pool is created. The component tends to bulge upward when heated because the material expands and exerts an expansion force outside the molten pool boundary.

However, the expansion is limited by the boundary and the surrounding material due to the temperature differential. Metal yields readily at high temperatures, therefore some of the thermal strain is transformed into plastic strain. As the heat source travels, a temperature gradient of up to 104 K/mm forms near the molten pool, rapidly cooling and hardening the pool at a rate of 103–107 K/s [16]. The materials surrounding the molten pool prevent it from shrinking during cooling and solidification. Furthermore, because some of the thermal strain is transformed into plastic strain during the heating phase, extra strain is needed to compensate during the molten pool's cooling process. This strain compensation and the mechanical properties of the material, which gradually increase as the temperature decreases, result in a high magnitude tensile residual stress near the molten pool [17]. For additively made components to have long-term performance, dimensional precision, and structural integrity, residual stresses must be understood and measured. These internal stresses may cause distortion, cracking, or premature failure during service or post-processing procedures if they are not properly assessed.

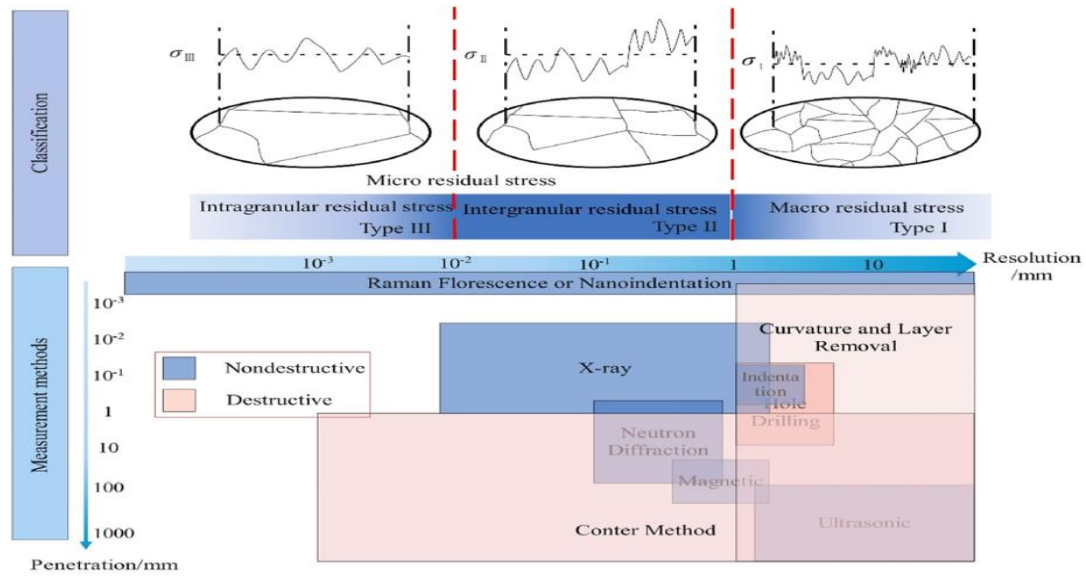


Figure 8: Classification and measurement method of residual stress [17]

1.5 XRD for Measurement of Residual Stress

One of the most popular and reliable methods for determining residual stress in crystalline materials, especially metals, is X-ray diffraction (XRD). Its foundation is Bragg's law, which states that a material's atomic planes scatter X-rays. The distance between these planes varies when residual stresses are present, which results in a change in the diffraction angle. This shift may be accurately measured in order to establish the material's strain, which is then utilized to compute the residual stress. This technique is ideal for sensitive or valuable components

because it is very accurate for surface-level stress analysis and doesn't involve the production of damaging samples [18].

Because of its high resolution, non-destructive nature, and direct correlation to crystallographic strain, XRD is regarded as superior to many other residual stress assessment techniques. For routine stress evaluation, XRD provides a more accurate and accessible alternative to methods like neutron diffraction, which necessitates specialized facilities, or hole-drilling, which needs partial material removal. It works particularly well for examining materials made using additive manufacturing, such as SS316L, where substantial surface tensions can be produced by quick heat cycles and solidification gradients. Because of this, researchers and engineers who want to guarantee the mechanical dependability and dimensional precision of additively built components use XRD [19].

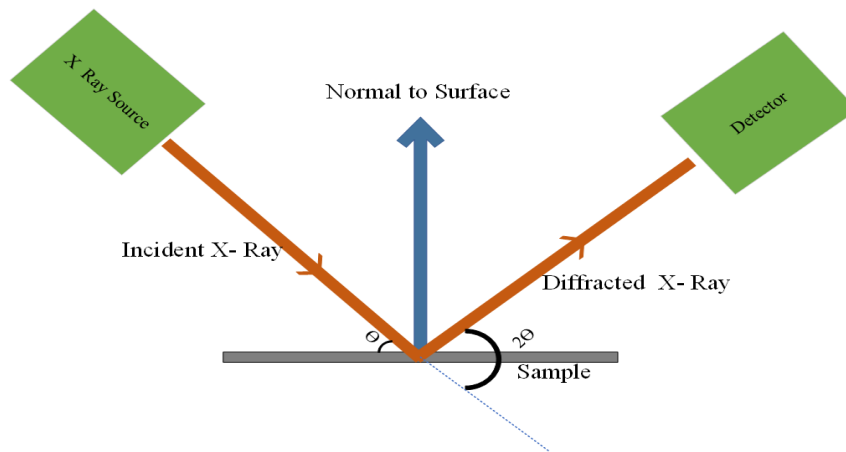


Figure 9: Schematic Diagram of XRD

Understanding the development of residual stress becomes critical for ensuring the structural integrity of fabricated parts. Since SS316L is widely used for its mechanical strength and corrosion resistance, analyzing the residual stress in this material can provide meaningful insights into the process-material interaction. In this study, an SS316L component manufactured using the LWDED process is examined.

CHAPTER 2

LITERATURE REVIEW

2.1 Metal Additive Manufacturing

In additive manufacturing (AM), the materials are deposited upon each other in layers repeatedly, joining them together under guidance from a 3D model to form the specified structure. This method allows rapid prototyping and the production of geometrically complex objects that cannot be made using conventional techniques. This type of manufacturing reduces manufacturing time and energy/material waste because it can manufacture goods on demand. The metal additive manufacturing industry has experienced a boom in 3D printer technology with very advanced machines and processes, but the number of metal alloys that are satisfactorily printed is small [7]. One of the well-known techniques of MAM is Laser Wire Direct Energy Deposition, in which Laser is used as a heat source to melt the metal in wire form. For the creation of intricate and big metal components, the wire-feed method is more appropriate [20]. Nevertheless, the technology is very much in the initial stages of development and is integrated into the industry on a large scale in progress very extensively and work is carried out to employ different materials.

Zafar et al. (2025) investigated that in metal additive manufacturing, choice of feedstock, whether powder or wire, has strong impacts on process efficiency, safety, and quality of part. Although powder-based approaches dominate, wire-feed processes have significant benefits. Wire-feed processes have superior deposition rates, up to 100% utilization of material, thus minimizing waste and cost. In contrast to powder systems that require sealed enclosures for prevention of harmful dispersion of fine particles, wire-feed processes are safer and more eco-friendly. In addition, wire-feed techniques are less limited by build size restrictions, enabling the production of larger pieces. These advantages make wire-feed additive manufacturing a better option for applications that require high efficiency and safety [21].

2.2 Laser Wire Direct Energy Deposition

A comprehensive review is conducted in this chapter to understand the working principle of LMDED, material used, process parameters, thermal modelling, melt pool

characterization, residual stress formation, etc. Solidification and microstructure theory regarding the laser wire feed DED technique has also been discussed.

La Pena et al., (2025) studied that melting metal wire with a focused laser beam as the wire is fed onto a substrate, Laser Wire Directed Energy Deposition (LWDED) builds up parts one layer at a time. It precisely controls deposition and utilizes minimal material. LWDED is safer, cheaper, and best suited for making or refurbishing heavy, high-strength parts with fewer mistakes compared to powder-based systems [22].

Based on Taghizadeh and Zhu (2024), Laser Wire Directed Energy Deposition (LWDED) is a common additive manufacturing method that is very efficient for the production of large-scale, high-performance products. The ability of LWDED to create parts with very good structural strength and low material loss is what the research indicates makes it valuable for use in heavy industries, aerospace, and energy. The results exhibit the benefits of LWDED, such as its high deposition rates, accurate heat control, and capability to treat a broad variety of metals, such as titanium, nickel alloy, and stainless steel. The process also supports near-net-shape manufacturing and mission-critical part repair, which shows its increasing application in ecologically friendly and cost-effective production. [23].

Ghasempour-Mouziraji et al. (2024) examined the effect of major process parameters on the stability and quality of Laser Wire Directed Energy Deposition (LWDED). It was discovered that higher laser power produced more profound and broader melt pools, enhancing fusion but also raising the likelihood of defect when the power is high. Beam diameter was particularly important in energy distribution, with large diameter resulting in shallow melt pools of uniform deposition and small diameter concentrated energy density, which could create porosity. Scanning speed's influence was such that increased speeds lowered unit length heat input, resulting in inadequate melting, whereas decreased speeds improved melt pool stability at the expense of overheating. Lastly, the study emphasized how the selection of scanning path, e.g., zigzag or oscillation patterns, assisted in controlling heat build-up, eliminating residual stress, and enhancing surface finish. The article emphasizes the importance of ensuring a balanced setting of these parameters for optimal build quality in LWDED [12].

Table 3: Effect of LWDED Process parameters

Parameter	Too Low	Optimal	Too High
Laser Power	Incomplete melting, poor bonding, low deposition rate	Stable melt pool, good bonding, consistent track formation	Excessive melting, keyholing, spatter, increased dilution, thermal distortion
Scanning Speed	Excess heat buildup, wider melt pool, possible distortion or sagging	Balanced heat input and track geometry	Incomplete melting, poor bonding, lack of fusion, bead discontinuities
Wire Feed Rate	Underfill, discontinuous bead, wire stubbing	Consistent and smooth deposition	Overfeeding, excess material, poor surface finish, possible balling
Laser Spot Diameter	High energy density, narrow bead, deeper penetration	Proper focus and coverage	Low energy density, wide and shallow melt pool, poor fusion
Layer Height	Lack of bonding with previous layer, poor build integrity	Proper layer bonding, good dimensional accuracy	Excessive layer height leads to weak bonding, possible delamination

2.3 Stainless Steel 316L in AM

Guaglione et al. (2024) discusses the use of Laser Wire Metal Deposition (W-LMD) in the manufacturing of 316L stainless steel parts, highlighting its usefulness in hybrid manufacturing. From the research, it is apparent that W-LMD is capable of manufacturing fully consolidated parts with over 99.9% density, which confirms its suitability for high-quality production at large scales. The authors observe that 316L stainless steel's superior corrosion resistance and mechanical properties render it highly suitable for W-LMD, allowing existing parts to be repaired and hard-to-form features to be built into new components. This aligns W-LMD with a promising technology for sustainable and efficient manufacturing in many industries [24].

Brubaker et al. (2022) have carried out a study of 316L stainless steel parts produced by Wire-Fed Laser Metal Deposition (WFLMD) and presented the superiority of the process over other

additive manufacturing processes. The study showed that parts produced by WFLMD attained relative densities greater than 98% and consisted of mainly austenitic microstructures but with some ferrite and carbide phases. Electron backscatter diffraction confirmed tilted or twisted grain structures, and mechanical testing confirmed that the strength and hardness of WFLMD-fabricated 316L stainless steel were as good as or better than those fabricated using other techniques. Fractography revealed ductile tearing with few defects, which means that WFLMD is a good technique for fabricating high-quality 316L stainless steel parts. The temperature gradient could result in residual stress formation in the components [25].

2.4 Heat Source Model

In their research, Kiran et al. (2022) investigated different heat source models for thermal simulation in metal Directed Energy Deposition (DED), with emphasis on their accuracy and computational cost. Among the most popular models, the Goldak double-ellipsoidal model provides a rigorous depiction of asymmetric heat distribution and is extremely apt for deep penetration and intricate thermal simulations. It splits the heat input into front and back ellipsoids, enabling accurate control of thermal gradients and melt pool characteristics [14].

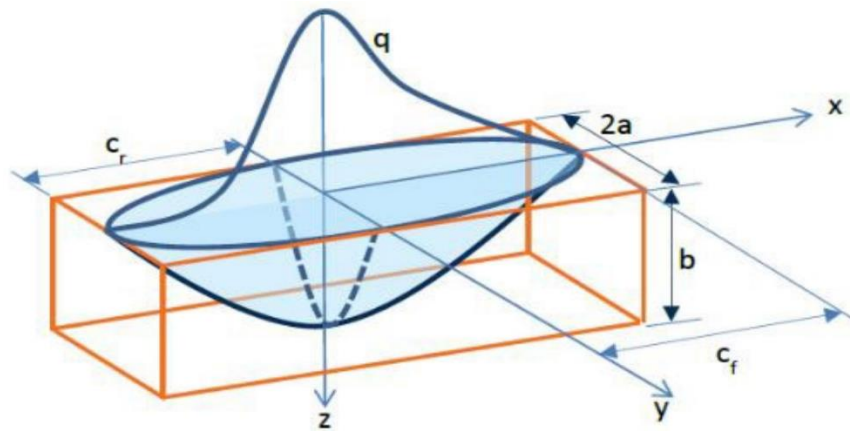


Figure 10: Goldak double ellipsoidal heat source [26]

The Gaussian heat source model, on the contrary, uses the assumption of a symmetrical energy distribution around the laser axis and has a simpler structure. It is less computationally demanding and suitable when a shallow and uniformly distributed melt pool is acceptable. The major difference is in complexity and accuracy, Goldak offers more physically realistic simulation but with the price of more computational effort, while Gaussian is chosen when quicker simulations are desirable without any major concession to accuracy. Owing to its compromise between simplicity and satisfactory precision, the Gaussian model is usually

preferred in applications such as parametric studies or initial-stage simulations where efficiency is essential [26].

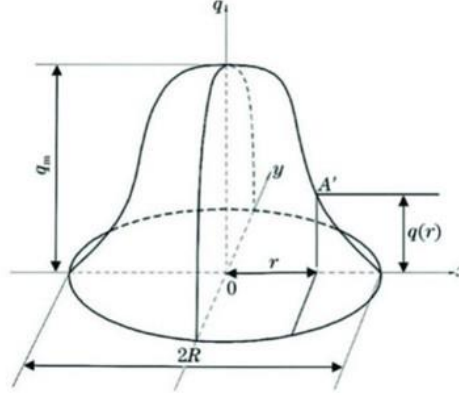


Figure 11: Gaussian heat source model [27]

The Gaussian heat source is defined by its radially symmetric distribution of thermal energy, peaking at the center of the laser beam and decreasing outward in a smooth Gaussian (bell-shaped) curve. This distribution is how real laser beams are, particularly continuous wave lasers, where energy is concentrated at the center and spreads evenly in all directions. The amount of heat input is regulated by factors like laser power, beam radius, and scanning velocity that affect the maximum heat intensity and thermal diffusion rate. Owing to its point-like nature, the Gaussian heat source suits the simulation of localized solidification and melting very well and hence finds extensive use in laser cladding, welding, and Directed Energy Deposition (DED) processes. Its smooth energy gradient also reduces numerical instabilities in thermal modelling and enables more convenient mathematical formulation and computational implementation [27], we have the heat flux $q(r)$ equation shown in Eq. 1,

$$q(r) = \frac{P}{\pi r_0^2} \exp\left(-\frac{r^2}{r_0^2}\right) \quad \text{Eq. 1}$$

2.5 Residual Stress

Zhang et al. (2024) present an extensive evaluation of the mechanics involved in the formation of residual stress in metal additive manufacturing (AM), with a focus on the challenge of cyclic thermal histories specific to processes such as Laser Wire Directed Energy Deposition (LWDED). Residual stresses are formed in the parts developed as a consequence of the high thermal gradients due to the rapid cycle of heating and subsequent cooling associated with the layer-by-layer deposition process, based on the research. These stresses degrade the parts' mechanical properties and dimensional accuracy, which can cause deformation and reduced

performance. The authors emphasize the significance of understanding these mechanisms in order to establish methods for reducing residual stress as well as improving the structural integrity and reliability of parts produced using AM [28].

Madariaga et al. (2025) examine the use of X-ray diffraction (XRD) in the measurement of residual stresses in additively manufactured parts, with a focus on its strengths and limitations. The research identifies XRD as a non-destructive method that can yield detailed information regarding residual stress distributions close to the surface of the material. Through the examination of the diffraction patterns, XRD is able to identify alterations in the lattice spacing, which are indirect measures of internal stresses. This ability renders XRD very helpful for assessing the integrity of additively manufactured components without incurring any damage. Nonetheless, the method has a limitation in measuring only on the surface and is not necessarily representative of the state of stress in the whole volume of the part. Over these shortcomings, XRD continues to be a useful technique in assessing residual stresses in additive manufacturing that will help in optimizing process parameters in order to improve part performance and reliability [29].

2.5.1 Bragg's Law

In real materials, which consist of a vast number of atoms arranged in periodic patterns, the interaction of X-ray beams with these atomic structures leads to a phenomenon known as interference. When X-rays are incident on such a material, they are scattered by the atoms. Depending on the specific interplanar spacing and the wavelength of the incoming radiation, this scattering can result in either constructive or destructive interference.

Constructive interference, which leads to observable diffraction peaks, occurs only in specific directions and is governed by Bragg's Law [19]. This fundamental law describes the condition under which reflected X-rays from different atomic planes reinforce each other, resulting in detectable diffracted beams. Importantly, the reflection does not happen solely at the surface atoms, but also involves atoms located deeper within the crystal structure, allowing the X-rays to probe a considerable depth of the material.

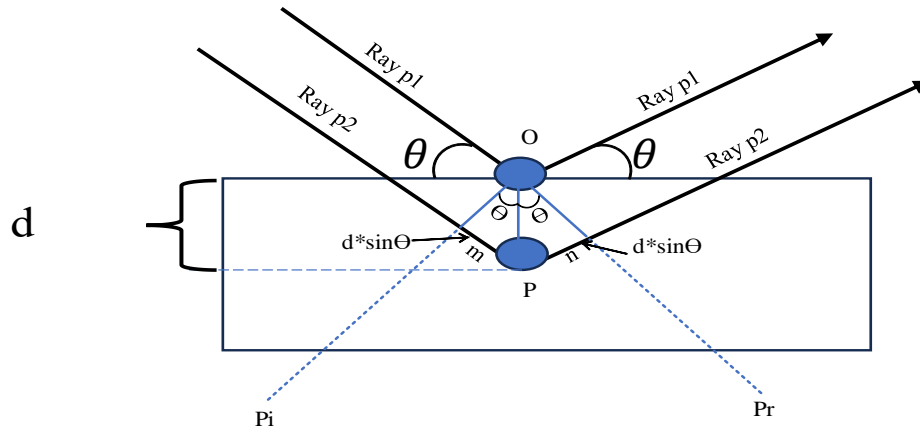


Figure 12: Diffraction of X-ray by a crystal

Figure 12: Diffraction of X-ray by a crystal illustrates the reflection of an X-ray beam from two ideal parallel lattice planes within a crystalline structure. In actual crystals, there are numerous such planes, but for simplicity, only two are shown here. The distance between these planes is known as the interplanar spacing and is denoted by d .

In the diagram, the lines P_i and P_r are perpendicular to the incident and reflected X-ray beams, respectively. The segment oP_i represents a wavefront of the incoming X-rays. For constructive interference to occur—resulting in a detectable diffracted beam—points such as o and m on this wavefront must remain in phase. This condition is met when the additional path travelled by the reflected beam, represented by the segment mpn , equals an integer multiple of the X-ray wavelength (λ). This can be mathematically expressed in Eq. 2:

$$mpn = n\lambda \quad \text{Eq. 2}$$

where n is an integer and λ is the wavelength of the X-rays. This relationship is a direct consequence of Bragg's Law, which governs the principles of X-ray diffraction in crystalline materials. The distances mp and np are equal to $d \sin \theta$. The distance mpn is $2d \sin \theta$. When this quantity is equated to $n\lambda$, we have Eq. 3:

$$\lambda = 2d \sin \theta \quad \text{Eq. 3}$$

- $n = 1, 2, 3, \dots$,
- λ – wavelength (1.5405 Å for Cu- K α Radiation)
- d - interplanar spacing
- θ - angle of reflection.

This Eq. 3 is known as Bragg's law. By employing a monochromatic X-ray beam of known wavelength and accurately measuring the diffraction angle (2θ), it becomes possible to determine the interplanar spacing d_{hkl} of crystal planes. This principle forms the foundation of both structural analysis and residual stress measurements in materials. Residual stress or strain analysis through X-ray diffraction is inherently based on Bragg's Law, and several fundamental assumptions underlie the method:

1. X-rays are treated as traveling waves, allowing wave interference principles to apply.
2. The path difference between X-rays scattered from successive planes is considered a linear function of interplanar spacing (d).
3. Scattering is elastic, meaning energy is conserved and there is no phase shift between incident and diffracted beams.
4. No multiple scattering is assumed within the specimen; that is, scattered X-rays do not undergo further scattering events (single-scattering approximation).

2.5.2 Diffractometer Geometry

The X-ray diffractometer is the most widely used instrument for obtaining diffraction patterns in crystalline materials. It is equipped with sensitive electronic detectors capable of measuring X-ray intensity, along with precision rotation stages that allow the manipulation of both the sample and the detector.

The basic working principle involves directing a monochromatic X-ray beam from the X-ray source onto the specimen, which is securely mounted on a sample holder. The holder is capable of rotating about the X-axis, which is perpendicular to the plane of the diffractometer, enabling various orientations of the sample to be analysed.

Simultaneously, the detector is positioned on a rotating arm that follows the circumference of the diffractometer, allowing it to capture diffracted beams at precise angles. Both the sample stage and the detector can be rotated with high angular accuracy, typically in the range of $\pm 0.005^\circ$ to $\pm 0.0005^\circ$, making it possible to detect even subtle changes in diffraction angles[30]. This arrangement forms the basis of the θ - 2θ scanning method, where the sample is rotated by θ and the detector by 2θ , allowing the identification of specific interplanar spacings via Bragg's Law.

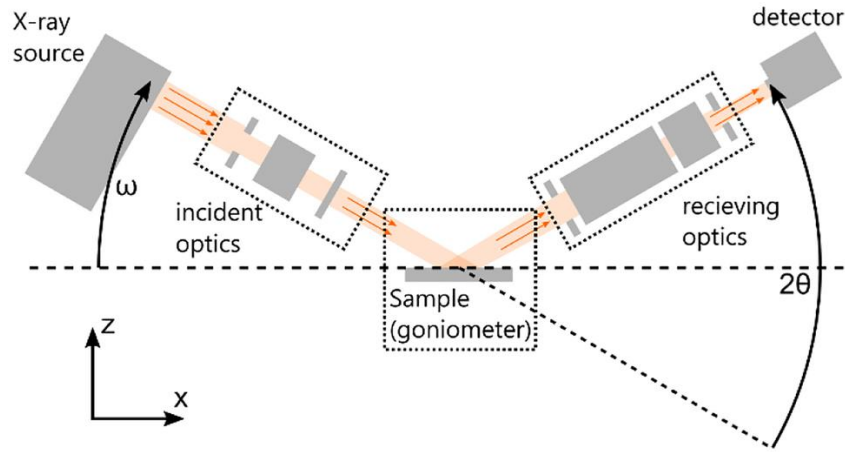


Figure 13: X-Ray diffractometer scheme [30]

In a diffractometer, both the incident and diffracted X-ray beams trace arcs along a focusing circle, ensuring that any divergence in the incident beam is corrected by convergence at the receiving slit. This geometrical arrangement enhances the precision of beam alignment and maximizes the detection of diffracted rays.

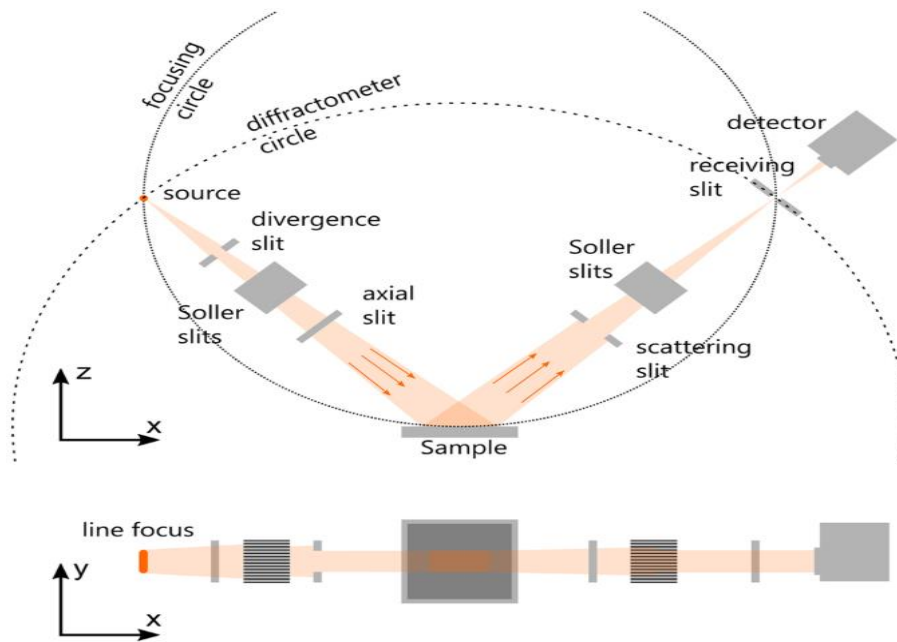


Figure 14: Focusing in the X-ray diffractometer [30]

The detection surface of the diffractometer is typically a cylindrical segment characterized by a fixed radius known as the radius of the diffractometer and height, which corresponds to the length of the receiving slit. The detector does not capture the entire diffracted beam but rather records only the portion that intersects this cylindrical surface.

To achieve an optimal balance between angular resolution and signal intensity, the receiving slit is usually designed as a rectangular aperture. This configuration ensures that the detector collects a consistent and well-defined portion of the diffracted beam, improving both resolution and counting efficiency.

2.5.3 Strain Measurement

To perform strain measurements using X-ray diffraction (XRD), the specimen is carefully mounted within an X-ray diffractometer and irradiated with a monochromatic X-ray beam. This beam interacts with the material's crystal lattice, producing diffraction patterns based on the atomic arrangement and interplanar spacing. As the diffractometer scans through an arc—typically with a radius corresponding to the geometry of the setup—the diffraction peaks are recorded at various angles. These peaks are essential for evaluating the internal strain present within the material.

A fundamental principle of this technique lies in the established relationship between the interplanar spacing of the crystal lattice and the resulting diffraction pattern. In an unstressed (strain-free) material, a unique and consistent diffraction pattern is produced, corresponding to its equilibrium atomic plane spacing. However, when the material experiences mechanical or thermal strain, distortions such as elongation or compression occur in the crystal lattice, which alter the interplanar spacing of specific $\{hkl\}$ planes.

These minute changes in spacing, denoted as d , lead to shifts in the diffraction peaks, as described by Bragg's Law. By accurately measuring the angular shift in the diffraction pattern and comparing it with the reference (strain-free) data, the change in interplanar spacing can be calculated. This shift provides a direct measurement of the strain within the material.

To interpret the strain quantitatively, it is necessary to establish mathematical relationships between the interplanar spacing and the observed strain. This involves correlating the measured diffraction angle 2θ with the spacing d_{hkl} for specific crystallographic planes, thereby enabling precise residual stress and strain evaluation.

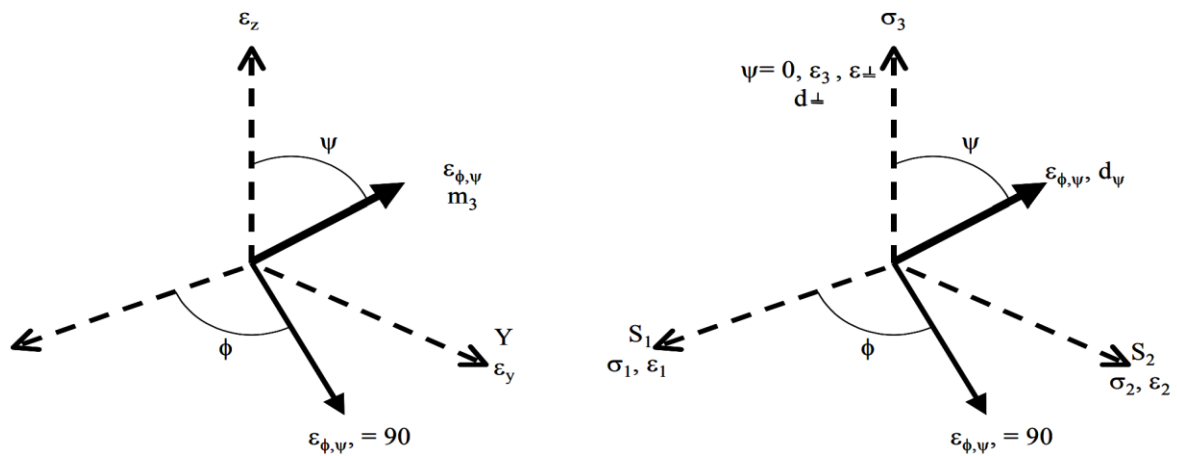


Figure 15: Co-ordinate system used for calculating surface strain and stresses [19]

Let us assume that, since the X-ray diffraction (XRD) measurement is conducted within a very shallow surface region, the normal stress in the out-of-plane direction (σ_3) is effectively zero.

However, the corresponding strain component, denoted as ε_z is not necessarily zero, due to Poisson's effect and redistribution of stress within the crystal lattice. If the unstrained interplanar spacing d_o is known (e.g., from a standard or stress-free reference sample), the strain ε in the direction normal to the diffracting plane can be calculated and represented in Eq. 4:

$$\varepsilon_z = \frac{d_n - d_o}{d_o} \quad \text{Eq. 4}$$

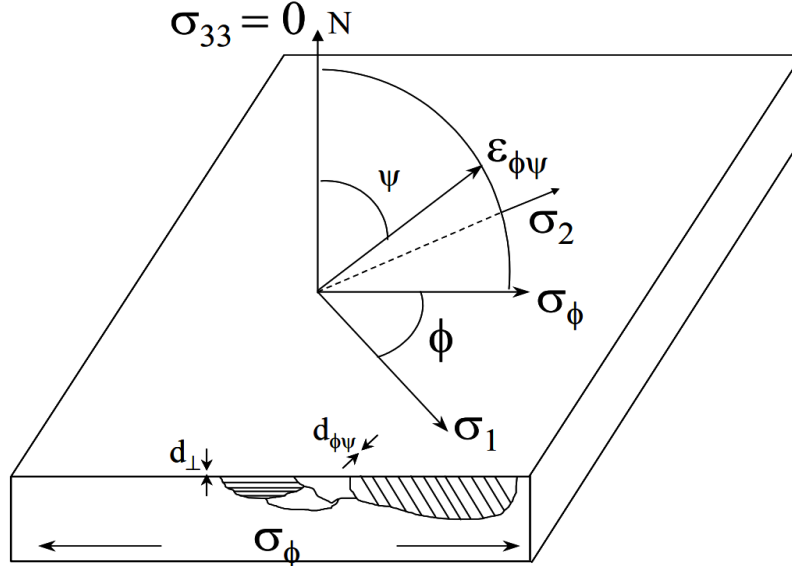


Figure 16: Schematic showing diffraction planes parallel to the surface and at an angle $\phi\psi$ [19]

Thus, the strain present within the surface of the material can be determined by comparing the interplanar spacing of a stressed sample with that of an unstressed (reference) sample. This requires precise measurement of the unstrained interplanar spacing (d_o), which can typically be obtained from a standard stress-free sample of the same material.

The basic strain calculation using XRD is valid for measurements taken normal to the sample surface. However, to obtain strain in other directions—especially in-plane residual stresses—the tilt angle ψ (psi) of the specimen within the diffractometer can be varied. By doing so, the diffraction from lattice planes inclined at an angle ψ to the surface can be analysed.

The strain ε_ψ in a direction inclined at angle ψ is calculated and represented in Eq. 5:

$$\varepsilon_z = \frac{d_n - d_o}{d_o} \quad \text{Eq. 5}$$

- d_ψ is the interplanar spacing measured at tilt angle ψ
- d_o is the unstressed interplanar spacing

2.5.4 Stress Determination

From Hooks' law, we know that the stress is calculated as shown in Eq. 6,

$$\sigma_y = E \varepsilon_y \quad \text{Eq. 6}$$

Assuming a state of plane stress exists, i.e., $\sigma_z = 0$, and that the stresses are biaxial, then the ratio of the transverse to longitudinal strains is Poisson's ratio, ν , is shown in Eq. 7;

$$\varepsilon_x = \varepsilon_y = -\nu \varepsilon_z = -\frac{\nu \sigma_y}{E} \quad \text{Eq. 7}$$

If we assume that at the surface of the material, where the X-ray measurement can be considered to have been made, that $\sigma_z = 0$, then we get Eq. 8,

$$\varepsilon_z = -\nu(\varepsilon_x + \varepsilon_y) = -\frac{\nu}{E}(\sigma_x + \sigma_y) \quad \text{Eq. 8}$$

Thus, we get the Eq. 9,

$$\frac{d_n - d_o}{d_o} = -\frac{\nu}{E}(\sigma_x + \sigma_y) \quad \text{Eq. 9}$$

If we consider the strains in terms of inter-planar spacing, and use the strains to evaluate the stresses, then it can be shown in Eq. 10

$$\sigma_\phi = \frac{E}{(1 + \nu) \sin^2(\psi)} \left(\frac{d_\psi - d_n}{d_n} \right) \quad \text{Eq. 10}$$

This equation enables the calculation of residual stress in a specific direction by evaluating the interplanar spacings obtained from two or more XRD measurements. These measurements are typically performed in a plane normal to the sample surface and aligned with the direction in which the stress is to be determined [19].

2.5.5 $\sin^2 \psi$ Method

In this case, experimental data is used to obtain the least-squares line. Then, the stress in σ_ϕ direction is the slope of the least-squares line, assuming material constants, E , ν , and unstressed d-spacing (d_0) are known. This method is known as $\sin^2 \psi$, because it utilizes multiple ψ values. The lattice spacing measured at $\psi = 0$ is substituted for d_0 in this experiment. This substitution

is based on the fact that, most of the materials, elastic strains do not introduce more than 0.1% difference between the true d_0 and d at any ψ . The error of such usage is less than 0.1%, because d_0 is a multiplier to the slope. Therefore, this much error is omitted. The stress can then be calculated from such a plot by calculating the gradient of the line and with basic knowledge of the elastic properties of the material. This assumes a zero stress at $d = d_n$, where d is the intercept on the y-axis when $\sin^2 \psi = 0$ [19], we get residual stress equation as Eq. 11,

$$\sigma_\phi = \frac{m}{d_0} \left(\frac{E}{1 + \nu} \right) \quad \text{Eq. 11}$$

Where m is the gradient of the d vs. $\sin^2 \psi$ curve.

To evaluate the residual stress, a linear fit must be applied to the data obtained from the d vs. $\sin^2 \psi$ plots for the top, middle, and bottom samples. This involves plotting the interplanar spacing (d) against the sine square of the tilt angle (ψ^2) and fitting a straight line through the data points [31].

The slope of the fitted line is then calculated for each sample. This slope value is crucial, as it helps determine the type and magnitude of residual stress present. A positive slope corresponds to tensile stress and a negative slope corresponds to compressive stress in the surface layer.

2.6 Objectives of the Study

The main aim of the present research is to explore the influence of Laser Wire Direct Energy Deposition (LWDED) process on the structural, mechanical, and compositional properties of SS316L stainless steel. The main aims are:

1. To experimentally quantify residual stresses in the LWDED-processed SS316L by X-Ray Diffraction (XRD) and cross-check results against existing literature.
2. To examine the microhardness of heat-affected and deposited zones, determining the change in mechanical properties with localized thermal effects.
3. To examine the microstructural features with Field Emission Scanning Electron Microscopy (FESEM) on grain refinement, melt pool morphology, and surface topography.
4. To compare with literature results and establish the viability of the LWDED process for additive manufacturing of SS316L parts with controlled residual stress and optimal mechanical properties.

CHAPTER 3

METHODOLOGY

3.1 Numerical Analysis

COMSOL Multiphysics 6.2 is used to simulate the temperature distribution. "Heat Transfer in Solids" is selected as the primary physics module in the description Wizard to accurately characterize the thermal behaviour. A time-dependent study design is done to account the heat source's mobility over time. In 2D, the workpiece is depicted as a rectangle with its height and length modified to match the proportions of the plate under investigation.

Material from COMSOL's library was assigned to the geometry. Precise thermal properties, such as density, specific heat capacity, and thermal conductivity, were derived from the available data and the temperature and time dependent equations in order to simulate realistic temperatures.

Heat Source node to the Heat Transfer in Solids interface is added to symbolize the laser or moving heat source. The heat source should be configured with a Gaussian profile in order to simulate the concentrated energy distribution of a laser beam. The beam's width and power were analysed to achieve the required melting temperature of SS316L on the surface. A time-dependent function is necessary to change the location of the heat source over the 2D surface over time. This can be achieved by adding a parametric expression that simulates the heat source's continuous movement in the x- or y-direction by determining the starting and stopping circumstances after defining the moving heat source. Typically, the initial temperature is set at ambient temperature. Boundary conditions were included to simulate real-world cooling, such as convective cooling at the edges. This makes it easier to replicate the heat dissipation behaviour realistically.

A finer mesh was done near the heat source and a coarser mesh farther away in order to capture fine-grained temperature variations. Solving the model once the mesh is set up to observe the heat distribution as the source travels throughout the 2D surface. Following the simulation, the temperature distribution is used to analyse the heat flow and thermal gradients. After the thermal solution. This 2D model offers an efficient and comprehensive view of the workpiece's response to the moving heat source.

Simulation Setup:

- Material: Stainless Steel 316L
- Laser Power: 1100 W
- Scan Speed: 7.5 mm/s
- Beam Diameter: 2.5 mm
- Ambient Temperature: 293.15 K

Simulation Duration: 15 seconds

3.2 Sample Fabrication

Using the Meltio M450 Laser Wire Direct Energy Deposition facility at IIT Bombay, the experiment was conducted. For superior metal 3D printing, the Meltio M450 is a wire-based directed energy deposition (DED) device that uses a wavelength of 976 nm. Through closed-loop feedback mechanisms, the machine provides fine control over deposition and has a multi-laser head that allows processing with metallic wires. In both industrial and research settings, this machine has been utilized extensively for additive manufacturing and is capable of producing near-net-shaped components with superior mechanical qualities.

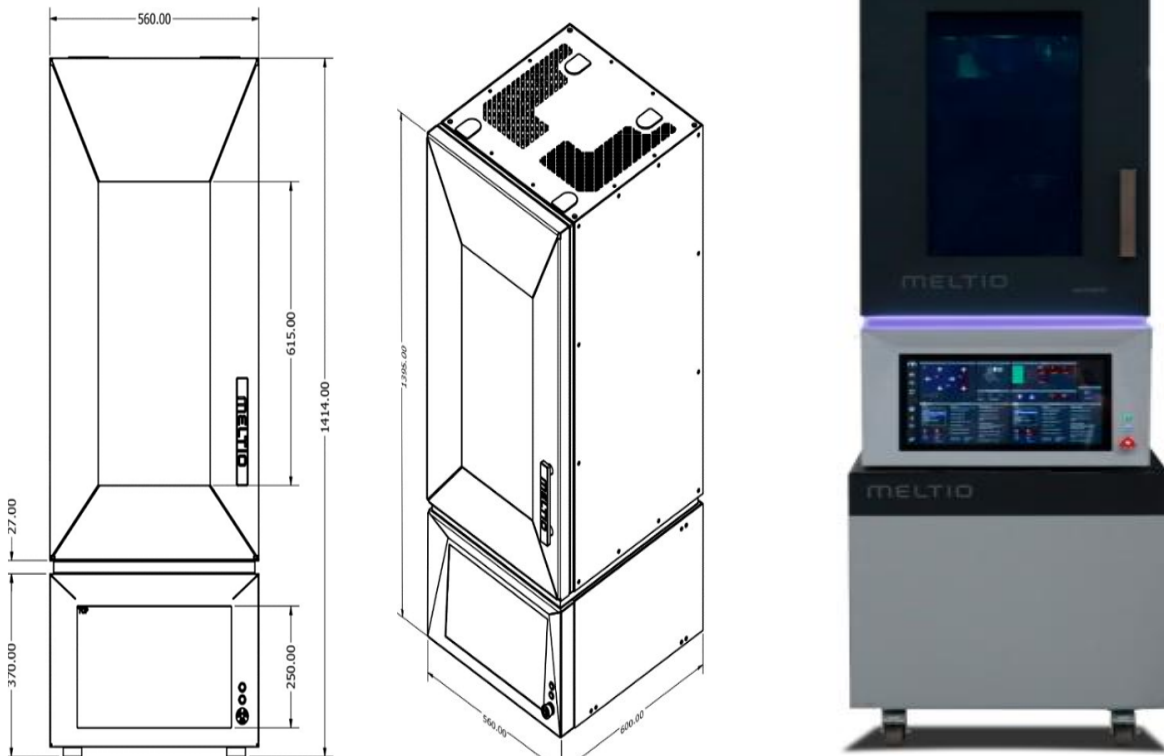


Figure 17: MELTIO M450

Table 4: Technical Specifications of MELTIO 450 [32]

Dimensions (WxDxH): 560 x 600 x 1400 mm	Power Consumption: 2 - 5 kW peak depending on selected
Print Envelope (WxDxH): 145 x 168 x 390 mm	Process Control: Closed-loop, laser and wire modulation
System Weight: 250 kg	Enclosure: Laser-safe, sealed, controlled atmosphere
Laser Type: 6 x 200 W direct diode lasers	Interface: USB, ethernet, wireless datalink
Laser Wavelength: 976 nm	Cooling: Active water-cooled chiller included
Total Laser Power: 1200 W	Wire Feedstock Diameter: 0.8 - 1.2 mm
Power Input: 208/230 V three-phase and 400V three-phase are compatible.	Wire Feedstock Spool: BS300

The 1.0 mm diameter stainless steel 316L wire utilized in this investigation complied with Meltio's requirements for the best system performance. For printing with stainless steel 316L, the process parameters include a laser power of 1100 W and a velocity of 7.5 mm/s. In order to guarantee high-density parts with few flaws, these specifications were established through intensive testing. With the lay direction kept at 0°, a zigzag toolpath method was used to construct a 25 mm × 25 mm × 25 mm cube. Simulation results and prior experimental data were used to determine the values of the parameters employed during the deposition process, such as laser power, scanning speed, wire feed rate, and laser spot size. A mild steel plate served as the deposition substrate, and it was firmly fixed on the build platform to guarantee stability during the printing procedure. The substrate surface was cleansed before deposition to get rid of any impurities that can compromise the build's quality. Following the toolpath produced by Meltio Horizon, the company's proprietary slicing software, the printing process was completed layer by layer.

Table 5: Printing Parameters for 316L

Technology	Laser Power [W]	Velocity [mm/s]	Layer Height [mm]	Layer Width [mm]	Wire Speed [mm/s]	Deposition Rate [g/h]	Volume rate [cc/h]
IR Laser 976 nm	1100	7.5	1.0	1.0	9.6	196	24.81

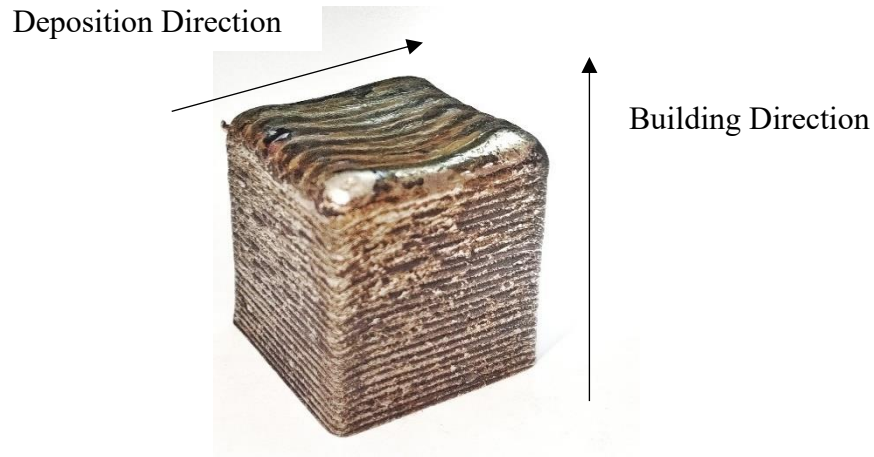


Figure 18: Additively Manufactured Part

After fabrication, the sample was sectioned at IIT Guwahati's Central Workshop utilizing wire-cut EDM (Electrical Discharge Machining). A rectangular block measuring 5 mm by 5 mm by 25 mm was taken out of one of the cube's corners as it was constructed. Molybdenum wire with a diameter of around 0.18 mm was utilized for EDM, which allowed for accurate and burr-free cutting of the metallic specimen without causing thermal damage to the microstructure.



Figure 19: (a)- Wire EDM Machine, (b)- Automatic Pneumatic mounting Press Machine

The cut section was subsequently separated into three segments, the top, middle, and bottom, each of which was roughly 5 mm thick, to enable thorough characterisation of the internal structure along the build direction. In order to examine the differences in microstructure and mechanical characteristics over the construction height, these segments were sectioned vertically, or parallel to the build height. This method aids in the analysis of possible gradients in hardness, porosity, particle size, and other properties brought on by layer-wise heat cycles during deposition.

An automatic pneumatic mounting press made by Chennai Metco was then used to install the top, middle, and bottom samples that had been vertically sectioned. The mounting procedure was done to make handling easier for the characterisation, polishing, and grinding that followed. In order to ensure adequate encapsulation and a flat, long-lasting surface appropriate for microstructural and hardness examination, the samples were put in a mould and implanted in a thermosetting resin under carefully regulated pressure and temperature.

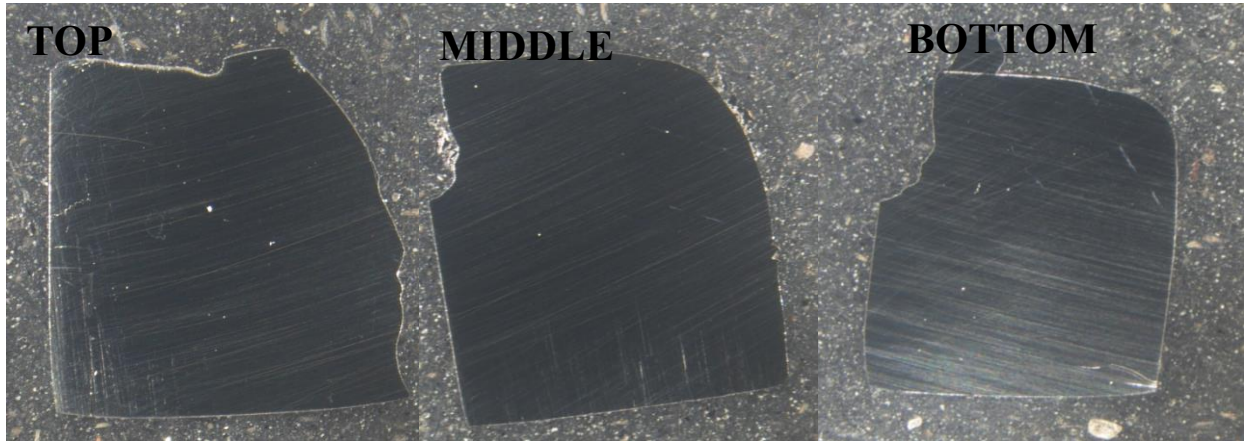


Figure 20: Moulded Sectioned Samples

The corner was selected to minimize the impact on the structural integrity of the remaining specimen while ensuring accessibility for post-process analysis. This location also represents a region where residual stress accumulation is often more pronounced due to uneven heat dissipation at the boundaries during deposition. Sectioning along the build direction was essential to capture the effects of layer-by-layer material addition and thermal cycling, which directly influence the development of microstructure and residual stress gradients throughout the height of the component. Analyzing this orientation provides critical insights into the vertical stress distribution and thermal history experienced by the part during the Laser Wire Directed Energy Deposition (LWDED) process.

3.3 Microhardness

Microhardness testing is a crucial method for assessing a material's localized hardness, particularly when a small sample size is required or when it's necessary to examine hardness differences throughout several regions. The quality and consistency of the manufactured object are crucially determined by microhardness testing in additive manufacturing techniques such as Laser Wire Direct Energy Deposition (LWDED). The sectioned portions taken from the manufactured SS316L block were subjected to microhardness tests in this investigation. To guarantee precise indentation and prevent surface flaws from influencing the results, the samples were appropriately polished to a mirror-like surface finish.

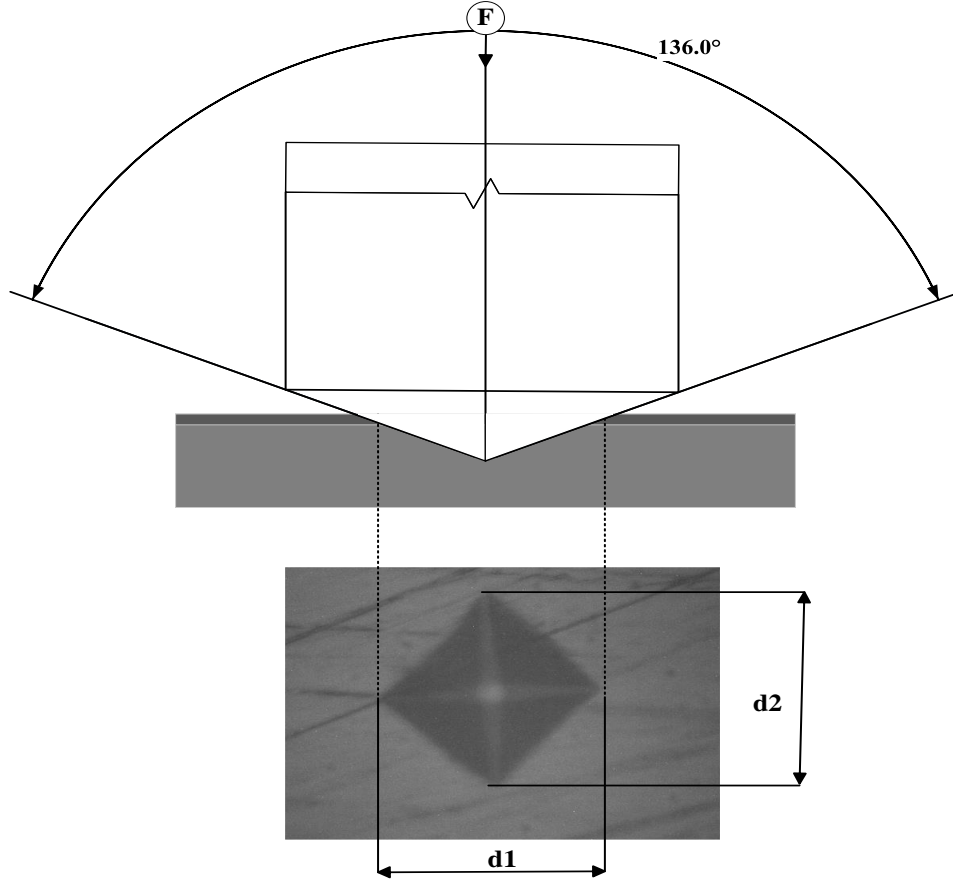


Figure 21: Schematic of the Vickers Microhardness method test

The measurements were made using a Vickers microhardness tester. This technique involves pressing a diamond-shaped indenter into the material surface for a predetermined amount of time while subjected to a particular load. The applied load and the indentation's area are used to determine the hardness value once the load has been removed and the two diagonals of the mark have been measured. A load of 300 grams-force (gf) was applied during the current job, and each measurement was dwelled for 20 seconds. The HVN can be calculated by Eq. 12,

$$HVN = 1.854 * \frac{F}{d^2} \quad \text{Eq. 12}$$

F = load value in gf

d = arithmetic mean of the two diagonals, in μm , $d1$ and $d2$

In order to create hardness profiles, a series of indentations were made. Understanding the mechanical property distribution over the part's height was made easier by the hardness values that were acquired. They also showed any abnormalities, such as soft or hard zones, that might have been caused by phase transitions, variations in cooling rates, or residual stresses during fabrication.

3.4 X-Ray Diffraction (XRD) for Residual Stress

A Bruker D8 ADVANCE ECO P-XRD diffractometer using Cu-K α radiation at a wavelength of 1.5406 Å was used for the measurements. The surface was carefully polished before testing to get rid of oxide layers and enhance the quality of the diffraction signal without changing the stress state.

The residual stresses were calculated using the $\sin^2\psi$ approach, which yielded a valid d vs. $\sin^2\psi$ curve by measuring several diffraction peaks at various tilt degrees (ψ angles). The amount and type (compressive or tensile) of the material's residual stress are closely correlated with the slope of this curve. To guarantee precise and sensitive measurements, care was made to choose a suitable diffraction plane and X-ray wavelength for SS316L. Standard stress calculation methods were used to assess the collected data, and suitable material constants, such as Young's modulus and Poisson's ratio for SS316L, were utilized. With this technique, surface residual stresses may be accurately determined without causing further sample degradation or modification. The foundation for assessing process dependability and the structural performance of the manufactured part is the XRD analysis results, which offer crucial information into the heat history and stress evolution during the LWDED process.

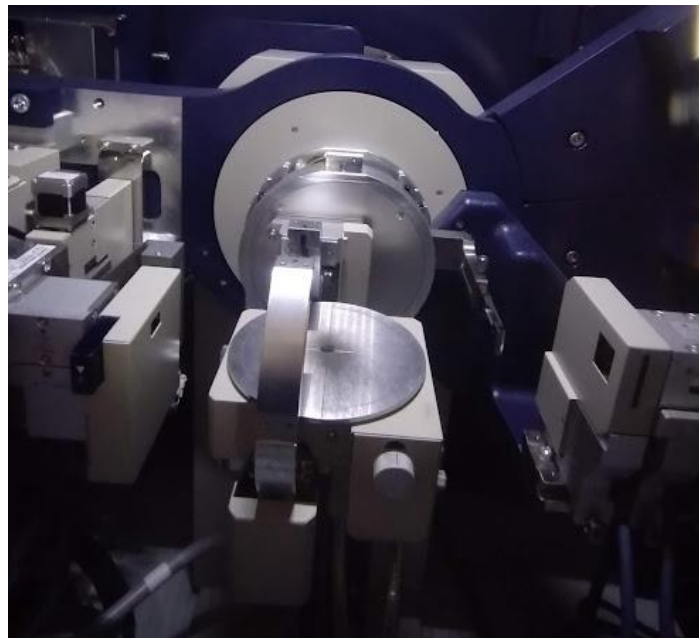


Figure 22: XRD facility at IITG

3.5 Field Emission Scanning Electron Microscopy (FESEM)

Field Emission Scanning Electron Microscopy (FESEM) is an advanced imaging technique that allows for very high-resolution observation of the surface and microstructural features of materials. It operates on the basis of scanning the sample surface with a concentrated electron beam and identifying the signals produced by interactions between the electron and the sample. After that, these signals are transformed into crisp pictures that show flaws, grain patterns, and surface topography at the micro and nanoscale levels.

The polished and etched cross-sections of the SS316L samples were subjected to FESEM examination in this investigation [33]. Studying the microstructural features, including grain shape, the existence of any microporosity, fissures, unmelted particles, and other flaws that might have developed during the deposition process, was the main objective of the FESEM. Compared to conventional optical microscopy, the method offered significantly greater magnification and improved depth of focus, which made it simpler to see minute microstructural details.

CHAPTER 4

RESULTS and DISCUSSION

4.1 Visual and Dimensional Inspection

The first and most fundamental step in assessing the quality of the manufactured sample is visual and dimensional inspection. It offers a rapid and efficient method of identifying any surface-level flaws in the deposited layers, including cracks, porosity, delamination, and abnormalities. This technique enables a preliminary assessment of the deposition strategy's process stability and efficacy, taking into account variables like wire feed rate, scanning speed, and laser power.

The manufactured SS316L block ($25 \times 25 \times 25 \text{ mm}^3$) used in this investigation was examined very away following deposition. The sample was visually inspected for any indications of surface irregularity, apparent porosity, or distortion. The total shape matched the anticipated dimensions and the deposited layers were found to be well-bonded, suggesting a stable melt pool and steady material flow throughout the construction process.

With an accuracy of $\pm 0.02 \text{ mm}$, dimensional measurements were taken with a Vernier calliper. To confirm dimensional accuracy and evaluate any deviation brought on by heat factors like shrinkage or residual stresses, the intended CAD model and the actual dimensions were compared. For the intended use, the observed departure from the planned size was negligible and within allowable tolerance levels.

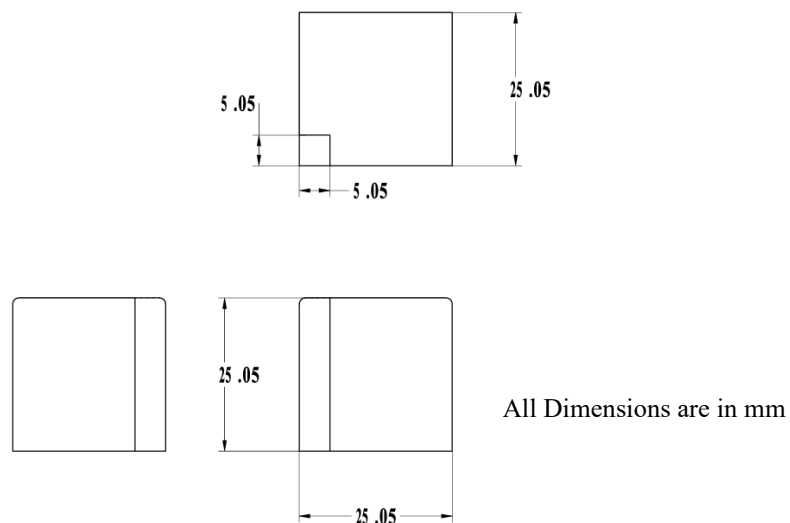


Figure 23: Draft for Wire Cut EDM

4.2 COMSOL Simulation

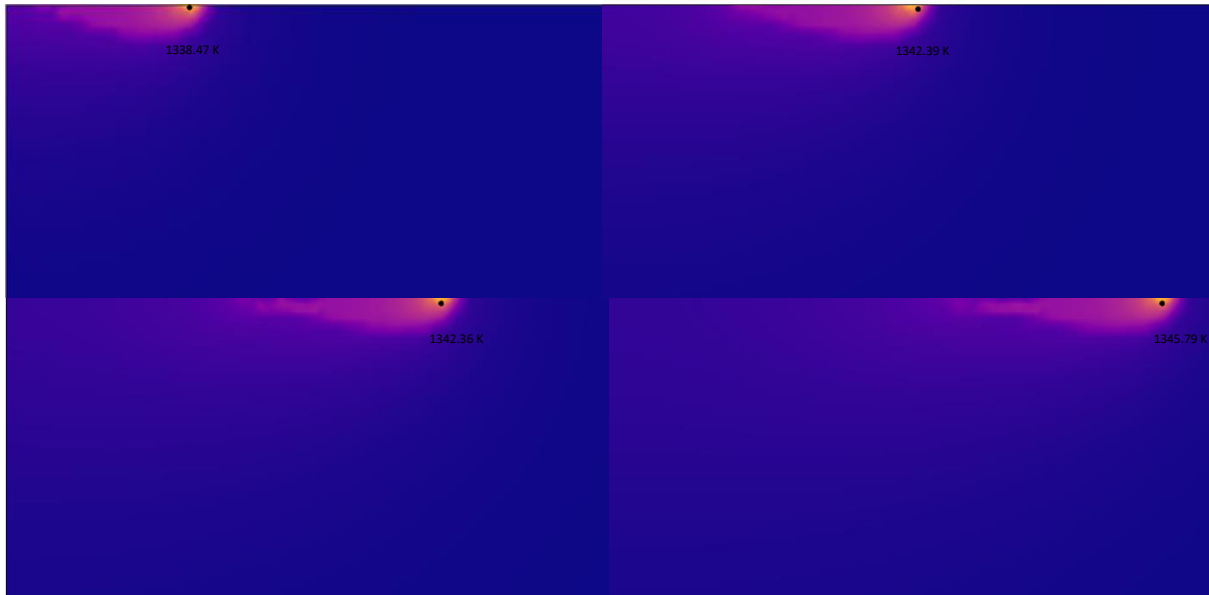


Figure 24: COMSOL- Melt pool Simulation

The melt pool simulation in Figure 24 demonstrates the dynamic material response to a translating laser heat source in the LWDED process. As the laser moves along the surface, a melt pool, or a region of local high temperature, tracks the movement. The simulation indicates the transient thermal field nature, with the maximum temperatures concentrated in the middle of the beam and a gradient outward. This is typical of the Gaussian heat source model, in which heat intensity decreases radially from the center. The moving heat source produces a steady-state thermal gradient, which is essential in evaluating thermal stress development and material properties after solidification. This thermal profile provides the basis for residual stress distribution prediction as well as the optimization of process parameters for enhanced build quality.

The temperature vs. time plot taken from the domain probe in Figure 25 shows the thermal state during the Laser Wire Directed Energy Deposition (LWDED) process. At first, the temperature increases rapidly, which marks the beginning of laser heating and the initiation of the melt pool. The temperature becomes steady at 1300 K, marking a steady-state condition where the material is kept molten by constant energy supply from the laser. This plateau verifies steady energy supply and effective heat absorption during dwell time. Following the departure or shut-off of the laser, a steep temperature drop is realized, which indicates the cooling stage, essential for solidification as well as microstructural evolution.

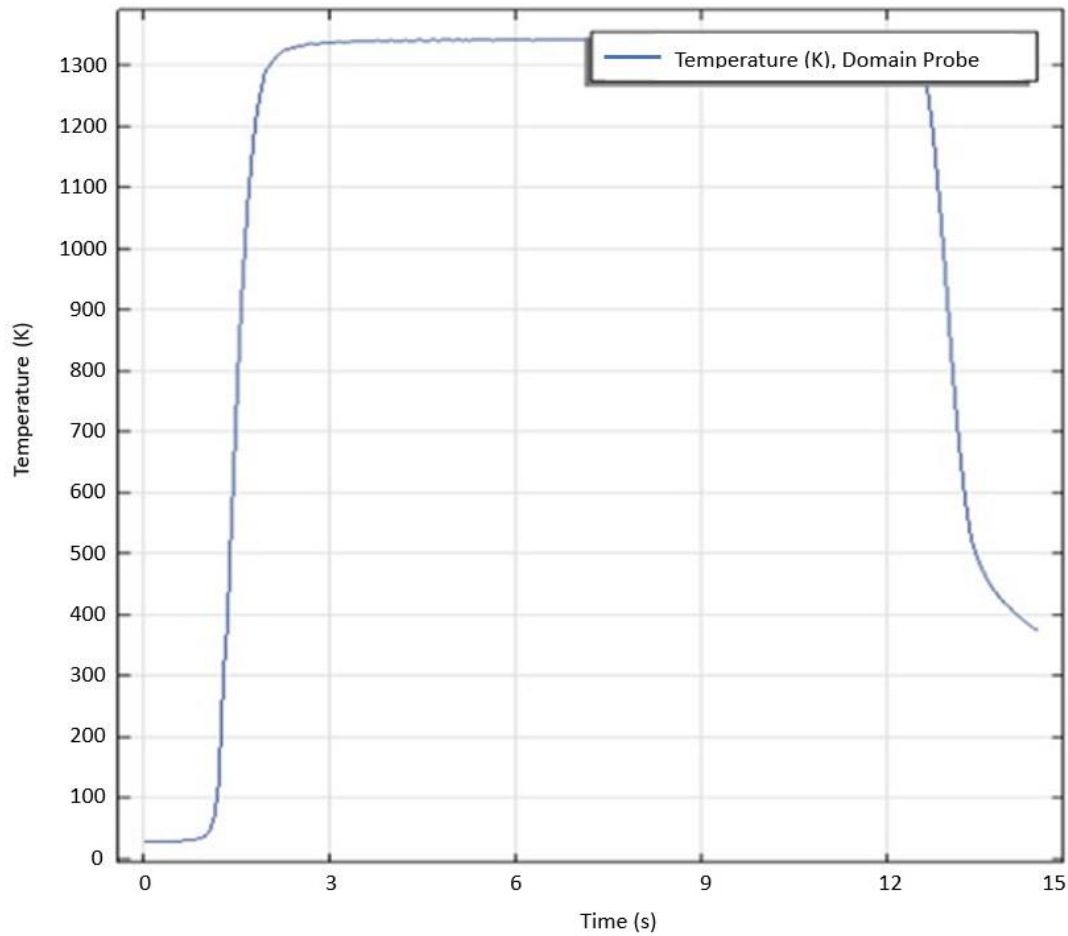


Figure 25: Temperature profile

4.3 Microhardness Analysis

The hardness values for the three samples in the build-up direction are displayed in the table at three separate locations. This pattern points to a significant variation in hardness across the build's height, which is probably caused by thermal gradients, cooling speeds, and numerous heat cycles throughout the LWDED procedure.

Table 6: Vicker Microhardness Values

	Top		Middle		Bottom
Location 1	209.91		239.749		220.22
Location 2	214.238		228.056		228.872
Location 3	213.507		254.249		214.972
Average	212.5517		240.6847		221.3547

It can be concluded that the hardness is higher in the center zone. However, because they were deposited last, the topmost layers may have seen slower cooling and less thermal cycling, which led to coarser grain structures and comparatively lower hardness. These findings demonstrate how process dynamics in Laser Wire Direct Energy Deposition affect the component's mechanical homogeneity. The obtained figures, which are 215 HV for 316L, are marginally higher than those provided by the supplier.

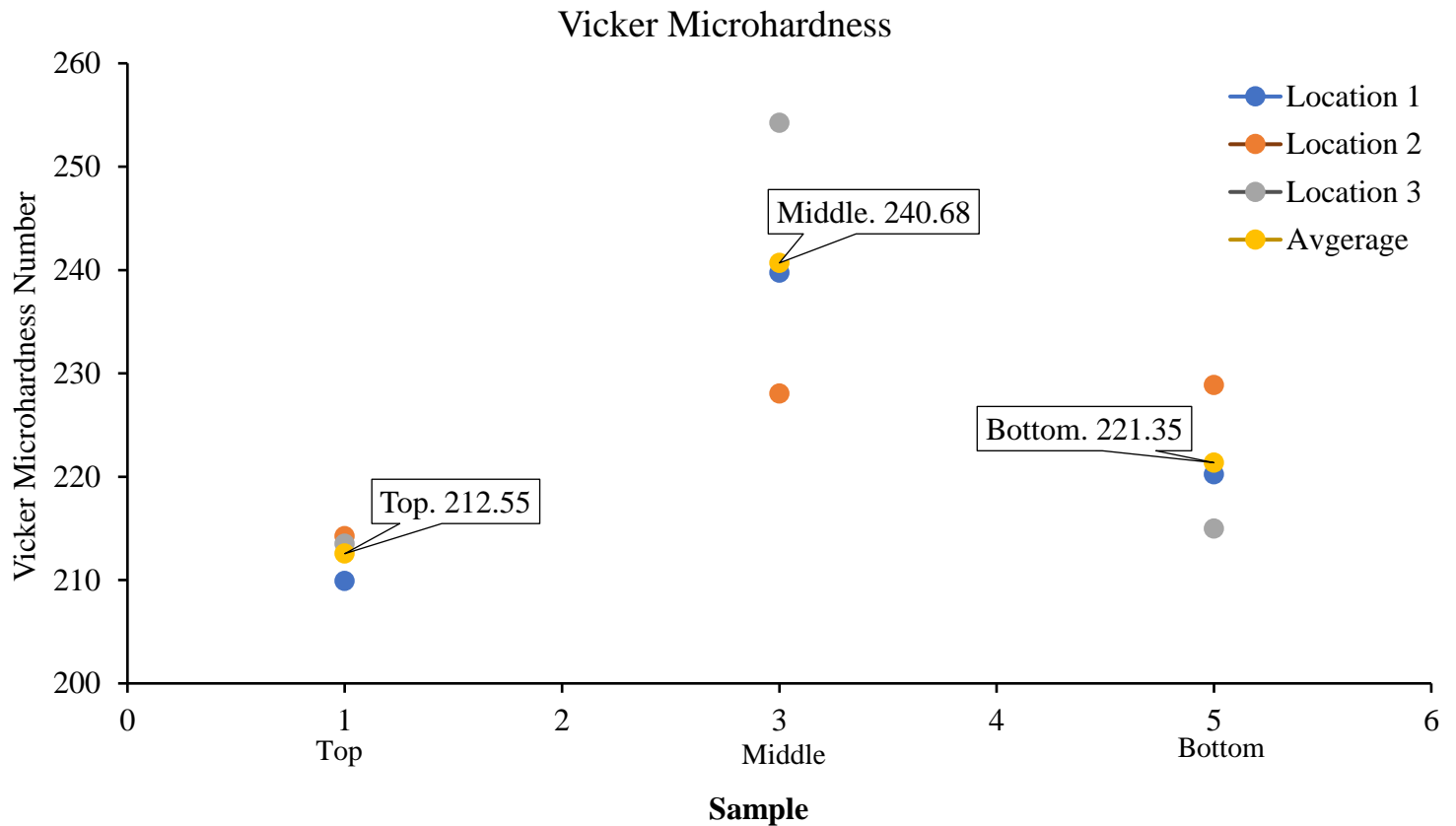


Figure 26: Vicker Microhardness Results

4.4 Analysis under FESEM

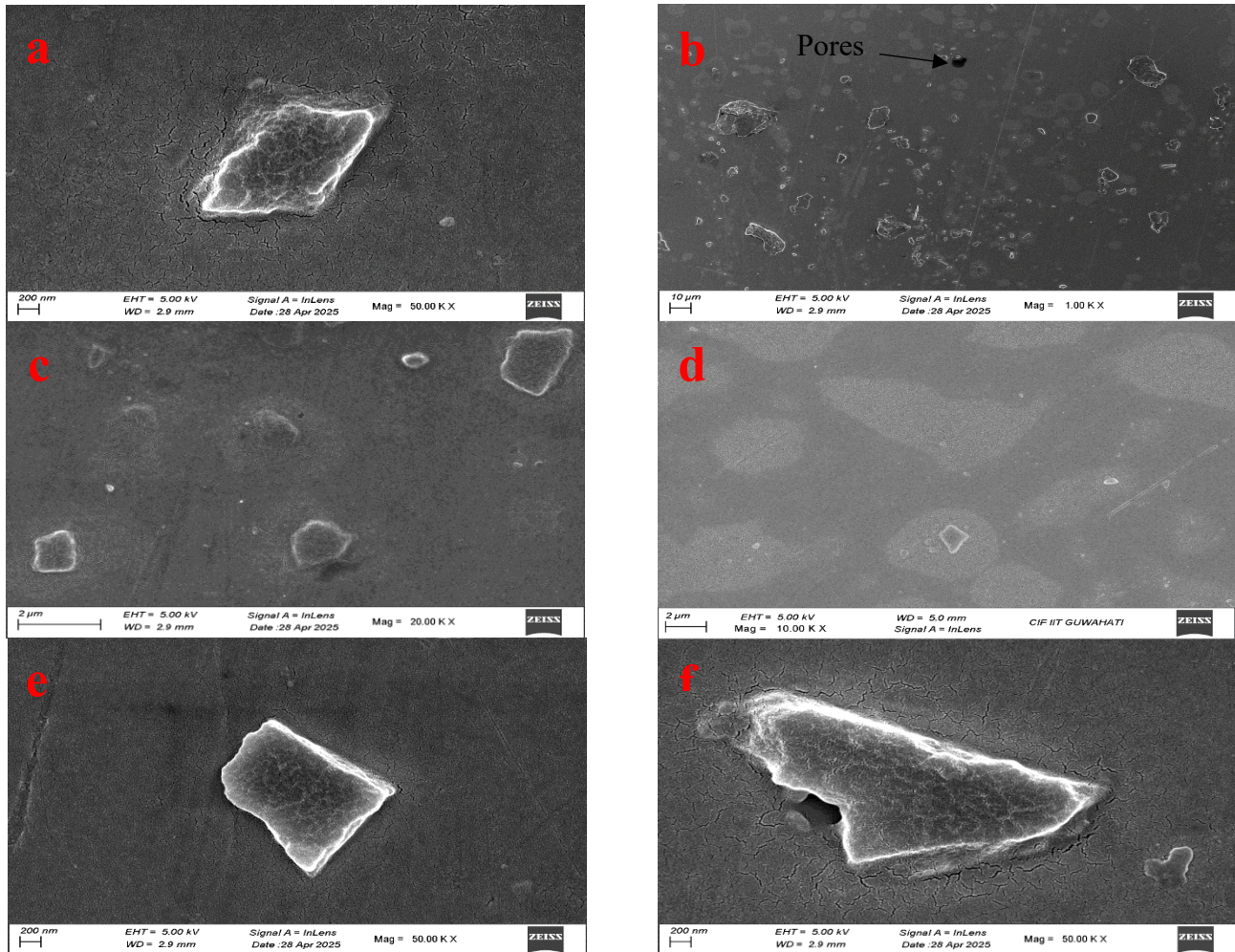


Figure 27: SEM Images of SS 316L

Nanoscale particles with sharp-edged morphologies and an average size of about 200 nm were found by FESEM investigation of the deposited surface. On the surface of the sample, these structures show up as solitary or grouped features. However, the absence of EDX analysis made it impossible to confirm the particles' chemical makeup. There is a consistent crystallographic texture in Figure 27 (d). Given the alloy system (SS316L) and the Laser Wire Directed Energy Deposition production conditions, these features might be delta ferrite (δ -ferrite) generated during rapid solidification. Previous investigations have demonstrated that delta ferrite can form in austenitic stainless steels produced under severe temperature gradients, particularly in welds or additive manufacturing builds. A few pores, which are regarded as microstructure flaws and usually arise from trapped gasses or incomplete fusion during the deposition process,

are shown in Figure 27 (b). These pores have the potential to concentrate stress and negatively impact the material's mechanical qualities, especially its ductility and fatigue strength.

4.5 XRD Results and Analysis

Analysis of the crystallographic phases of the materials was the first step in the XRD study. Figure 19 shows the diffractograms of the samples produced with Cu-K α radiation; the SS 316L samples only had austenitic peaks.

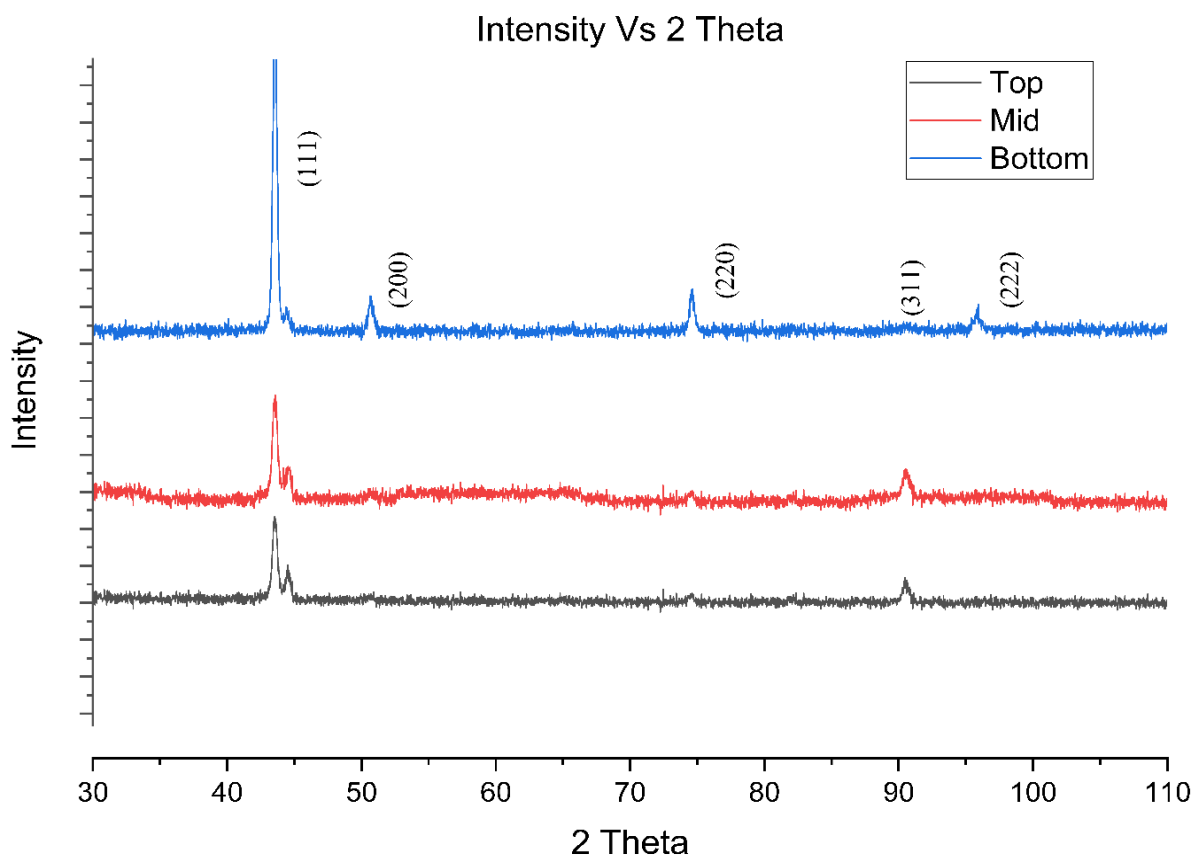


Figure 28: Diffractograms

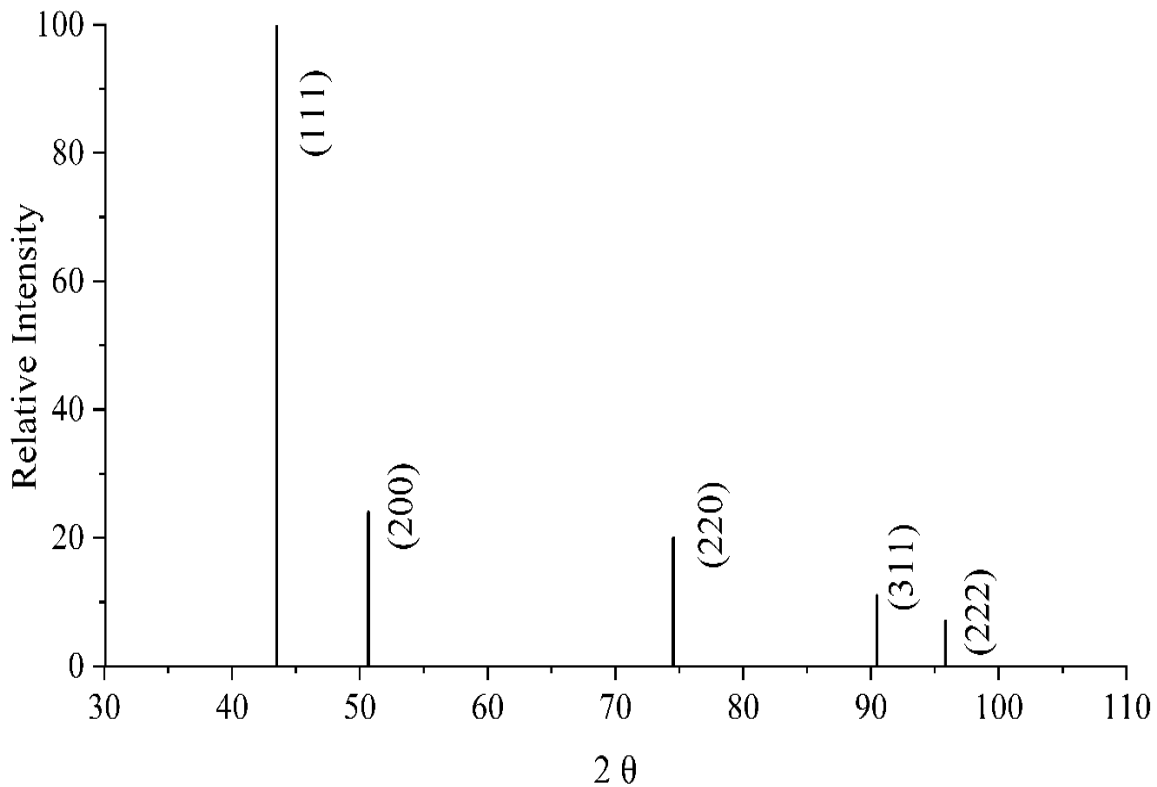


Figure 29: XRD peaks of reference material

The top, middle, and bottom sections of the manufactured SS316L sample were subjected to X-ray diffraction (XRD) investigation in order to look into differences in residual stress and crystallographic structure. For comparison examination, the diffraction patterns for each of the three regions were displayed on a single 2θ vs. intensity graph. Austenitic stainless steel's face-centered cubic (FCC) structure was represented by the peaks, which showed noticeable reflections at 74.5° , 95.7° , and 90.54° , which are generally connected to the (111), (200), and (220) planes, respectively. Variations in lattice strain caused by heat gradients and residual stresses along the construction height are suggested by the slight shifts in peak positions seen between the top, middle, and bottom samples. These distinctions are essential to comprehending how microstructural evolution is impacted by layer-by-layer deposition.

Table 7: d-value at $\psi=0$

No.	2Theta	d-Value	Intensity	h	k	l
1	43.49	2.079	100	1	1	1
2	50.67	1.8	24	2	0	0
3	74.54	1.272	20	2	2	0
4	90.46	1.085	11	3	1	1
5	95.82	1.038	7	2	2	2
6	117.72	0.9	2	4	0	0
7	137.68	0.826	8	3	3	1
8	146.23	0.805	5	4	2	0

XRD scans were performed at a ψ tilt angle of 0° to make residual stresses easier to calculate, and the samples' matching 2θ peak positions were noted. Bragg's Law was used to determine the interplanar spacing values (d_0) in Table 7 from these peaks. When the sample is tilted during additional measurements, these d_0 values, which indicate the strain-free lattice spacing in the direction normal to the surface, are used as a reference for determining strain. A comparison of these numbers sheds light on how the initial lattice spacing varies across the deposited sample's heights, most likely as a result of variations in cooling speeds and thermal histories across the additive manufacturing process. When evaluating residual stress later on using the $\sin^2 \psi$ technique, these baseline d_0 values are essential inputs.

4.5.1 Residual Stress in Top sample

The XRD scan of the top sample, carried out at multiple tilt angles (ψ), revealed a prominent diffraction peak around 74.5° .

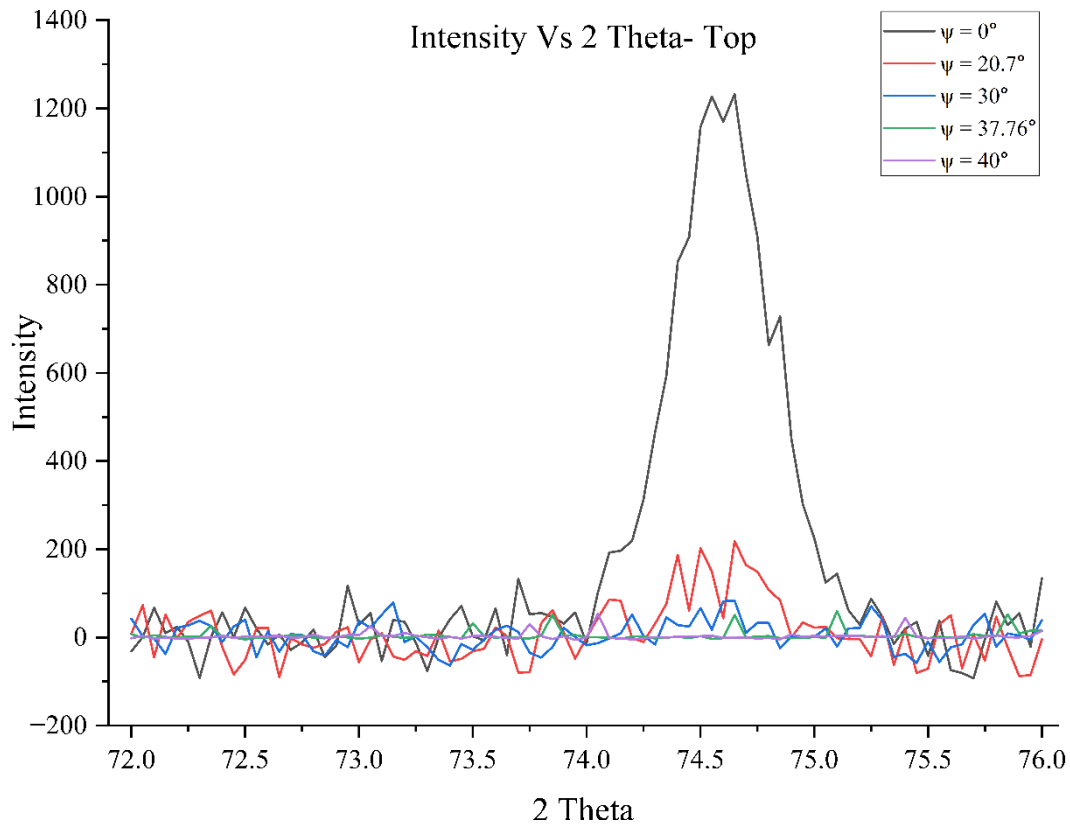


Figure 30: XRD peaks for Top sample, shifting of peak at 74.5°

The values in Table 8 show the maximum relative intensity and the corresponding values of the diffraction angle along with the d-spacing value.

Table 8: X-ray diffraction results for Top sample

ψ	$\sin^2(\psi)$	2θ	Intensity	θ	$d=\lambda/(2*\sin(\theta))$
0	0	74.65	1232.67	37.325	1.271408
20.7	0.125	74.65	218.6858	37.325	1.271408
30	0.25	74.65	83.63793	37.325	1.271408
37.76	0.375	75.1	59.92676	37.55	1.264904
40	0.413176	74.05	53.66542	37.025	1.280217

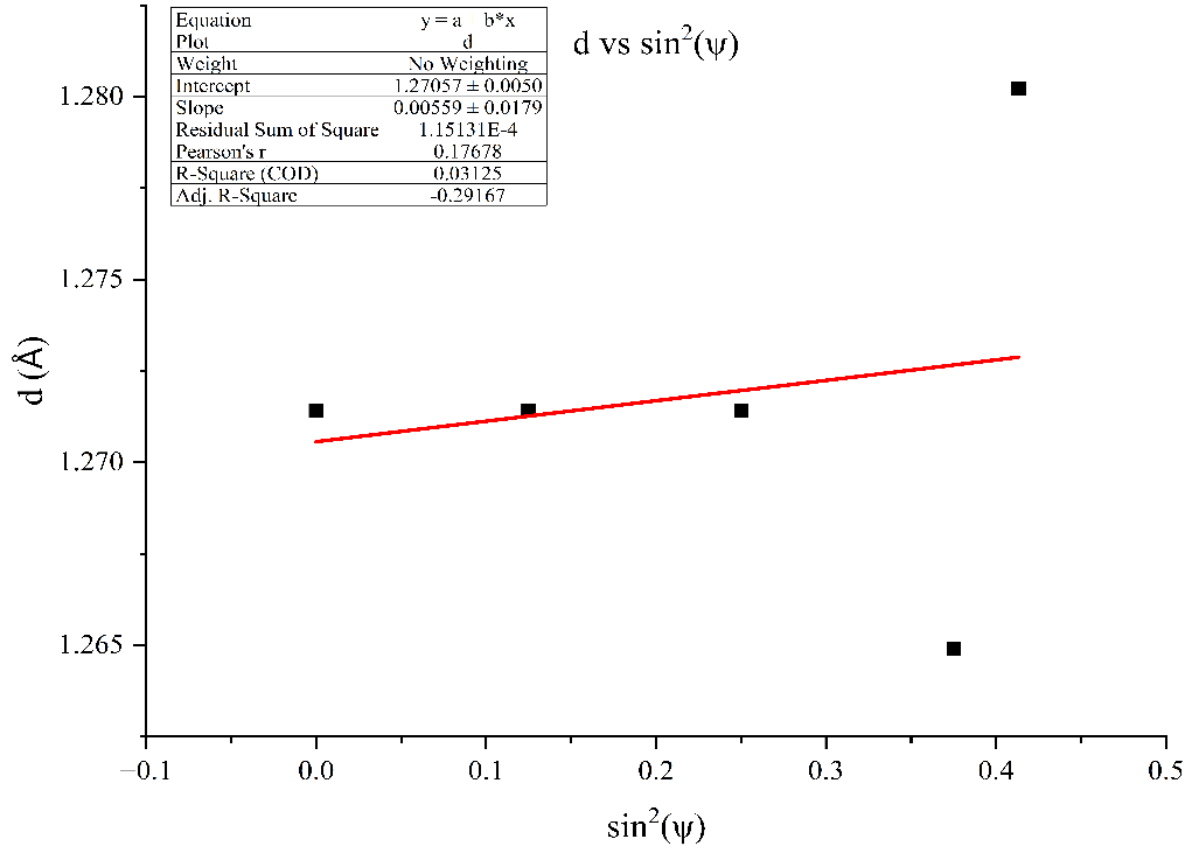


Figure 31: d versus $\sin^2\psi$ linear fitted graph

The resulting plots showed a linear relationship, confirming the applicability of the $\sin^2\psi$ method for stress determination. A linear fit was applied to the data, and the slope of the fitted line was found to be 0.0056 for the top sample. Positive slope corresponds to tensile stress within the measured surface layer. By using Eq. 11,

$$E = 193 \text{ GPa}, \nu = 0.3, m = 0.0056, d_0 = 1.272 \text{ Å}$$

$$\sigma_\phi = \frac{m}{d_0} \left(\frac{E}{1 + \nu} \right)$$

$$\sigma_\phi = \frac{0.00556}{1.272} * \left(\frac{193}{1 + 0.3} \right)$$

$$\sigma_\phi = 653.604 \text{ MPa (Tensile)}$$

4.5.2 Residual Stress in Middle sample

The XRD scan of the middle sample, carried out at multiple tilt angles (ψ), revealed a prominent diffraction peak around 95.7° .

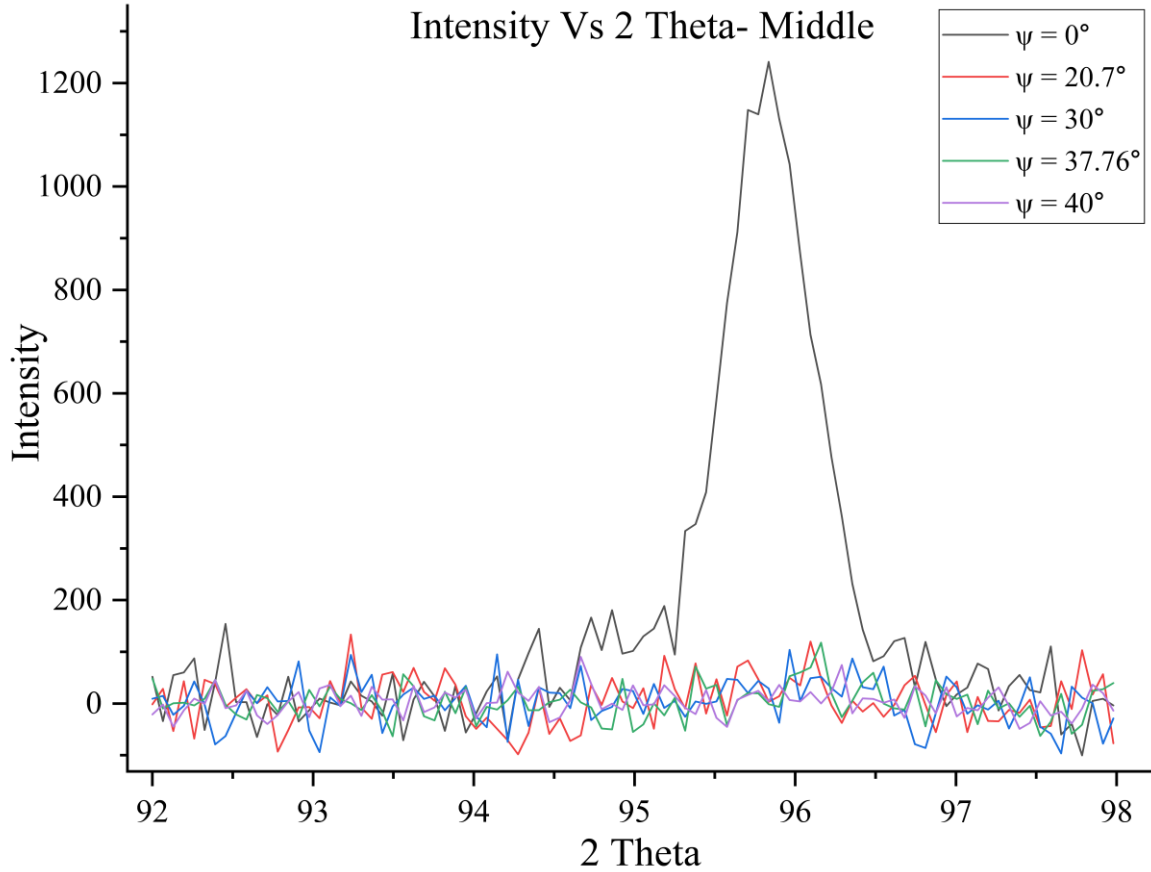


Figure 32: XRD peaks for Middle sample, shifting of peak at 95.7°

The values in Table 9 show the maximum relative intensity and the corresponding values of the diffraction angle along with the d-spacing value.

Table 9: X-ray diffraction results for Middle sample

ψ	$\sin^2(\psi)$	2Θ	Intensity	Θ	$d=\lambda/(2*\sin(\Theta))$
0	0	95.835	1241.121	47.9175	1.037888
20.7	0.125	93.235	133.4259	46.6175	1.059874
30	0.25	95.965	103.7741	47.9825	1.036826
37.76	0.375	96.16	117.8448	48.08	1.03524
40	0.413176	94.665	90.0816	47.3325	1.047601

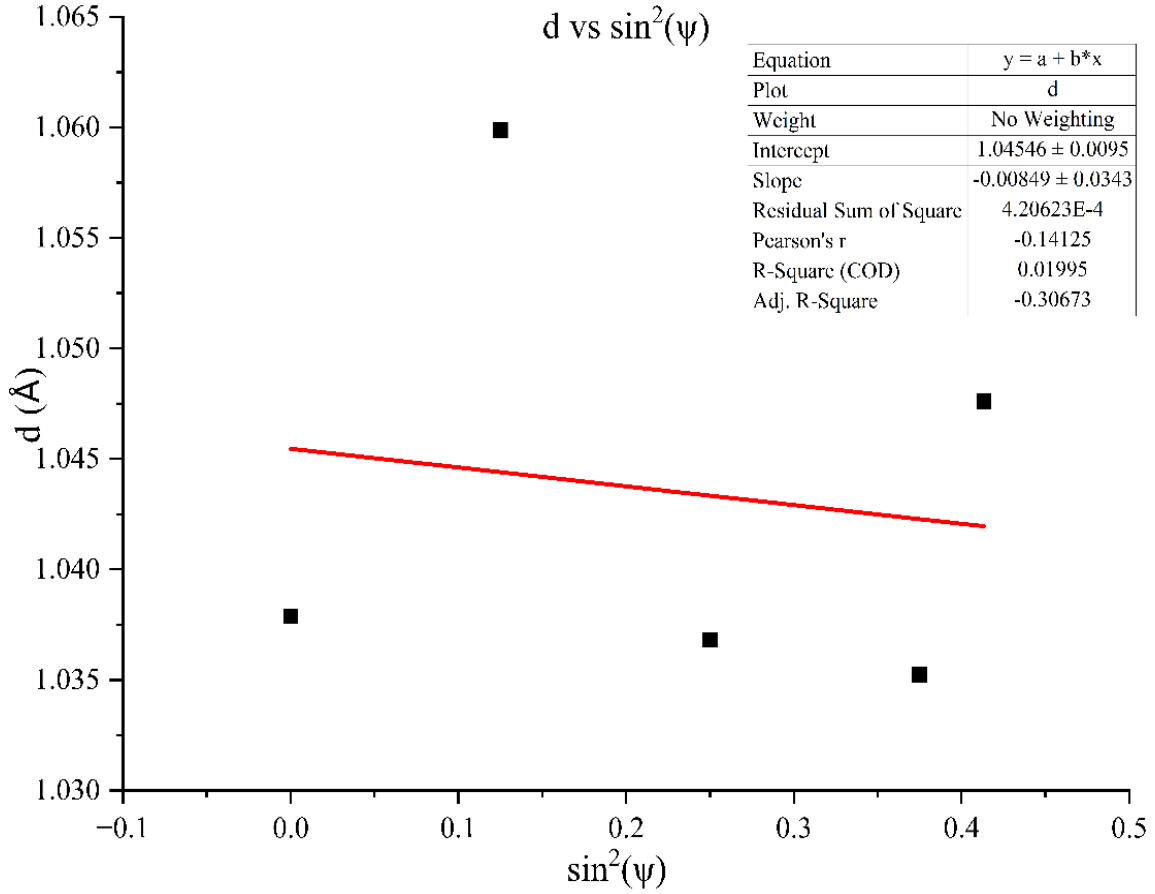


Figure 33: d versus $\sin^2\psi$ linear fitted graph

The resulting plots showed a linear relationship, confirming the applicability of the $\sin^2\psi$ method for stress determination. A linear fit was applied to the data, and the slope of the fitted line was found to be -0.0085 for the middle sample. Negative slope corresponds to compressive stress within the measured surface layer. By using Eq. 11,

$E = 193 \text{ GPa}$, $\nu = 0.3$, $m = -0.0085$, $d_0 = 1.038 \text{ Å}$

$$\sigma_\phi = \frac{m}{d_0} \left(\frac{E}{1 + \nu} \right)$$

$$\sigma_\phi = \frac{-0.0085}{1.038} * \left(\frac{193}{1 + 0.3} \right)$$

$$\sigma_\phi = -1215.7 \text{ MPa (Compressive)}$$

4.5.3 Residual Stress in Bottom sample

The XRD scan of the bottom sample, carried out at multiple tilt angles (ψ), revealed a prominent diffraction peak around 90.45° .

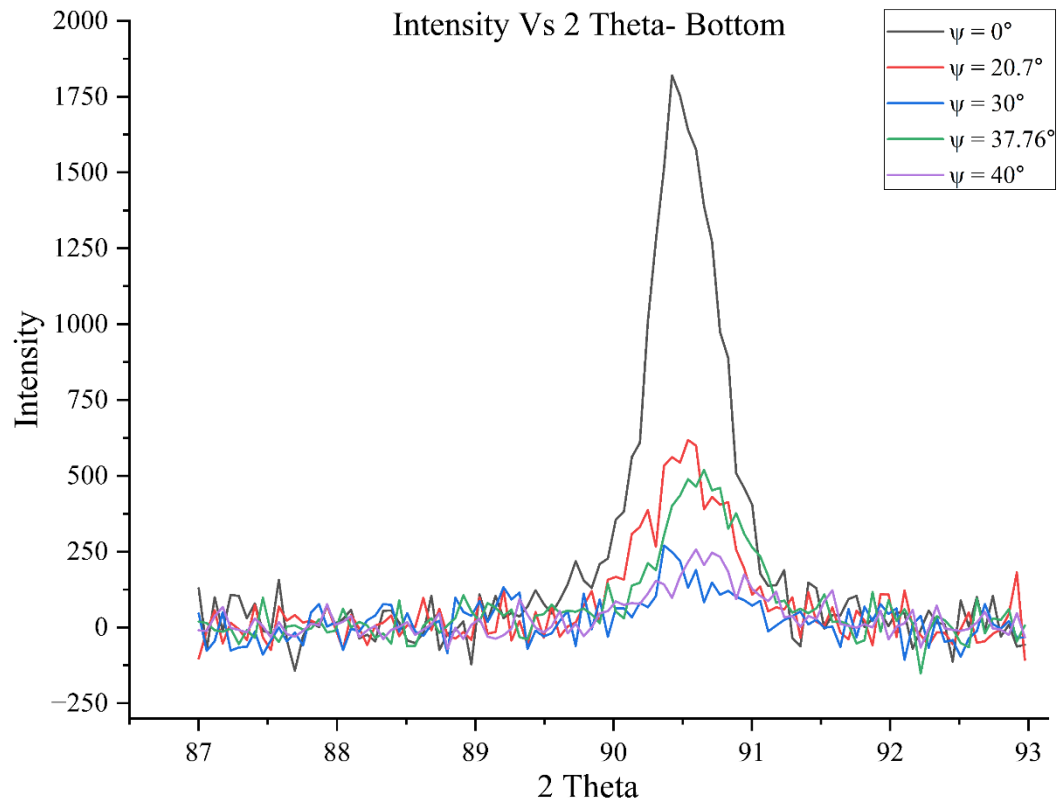


Figure 34: XRD peaks for Top sample, shifting of peak at 90.45°

The values in Table 10 show the maximum relative intensity and the corresponding values of the diffraction angle along with the d-spacing value.

Table 10: X-ray diffraction results for Bottom sample

ψ	$\sin^2(\psi)$	2Θ	Intensity	Θ	$d=\lambda/(2*\sin(\Theta))$
0	0	90.422	1819.95	45.211	1.085379
20.7	0.125	90.538	618.0249	45.269	1.08429
30	0.25	90.364	270.3831	45.182	1.085925
37.76	0.375	90.654	519.188	45.327	1.083204
45	0.5	90.596	257.4439	45.298	1.083747

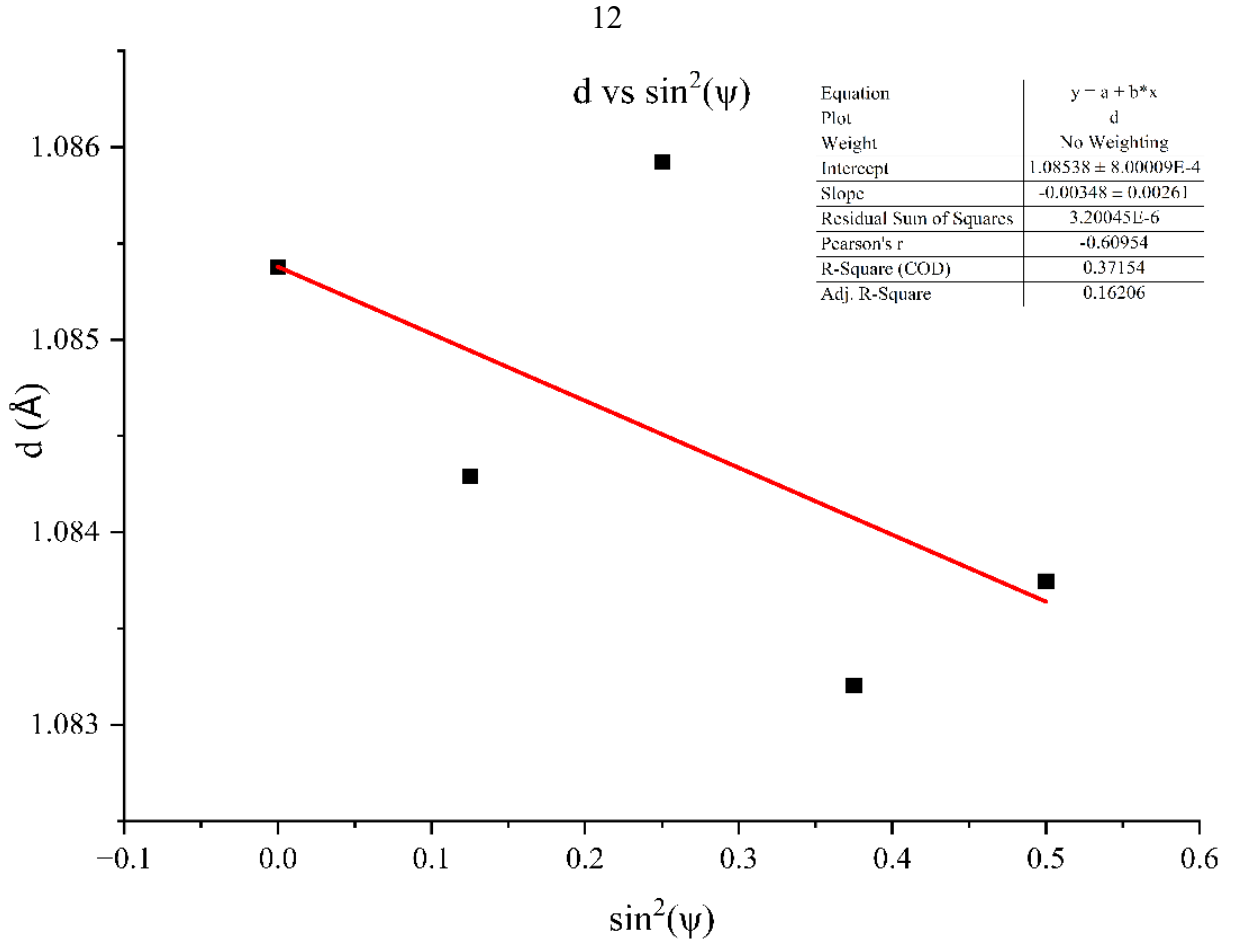


Figure 35: d versus $\sin^2\psi$ linear fitted graph

The resulting plots showed a linear relationship, confirming the applicability of the $\sin^2\psi$ method for stress determination. A linear fit was applied to the data, and the slope of the fitted line was found to be -0.0085 for the middle sample. Negative slope corresponds to compressive stress within the measured surface layer. By using Eq. 11,

$E = 193 \text{ GPa}$, $\nu = 0.3$, $m = -0.0035$, $d_0 = 1.085 \text{ Å}$

$$\sigma_\phi = \frac{m}{d_0} \left(\frac{E}{1 + \nu} \right)$$

$$\sigma_\phi = \frac{-0.0035}{1.085} * \left(\frac{193}{1 + 0.3} \right)$$

$$\sigma_\phi = -478.7 \text{ MPa (Compressive)}$$

CHAPTER 5

CONCLUSION

The Meltio M450 machine was utilized in this project to create and test stainless steel 316L parts. To understand its mechanical properties and the tension locked inside it after printing, a cube-shaped sample measuring $25 \times 25 \times 25 \text{ mm}^3$ was constructed and subjected to several experiments. To perform X-ray diffraction (XRD) and microhardness tests, the sample was divided into three sections: top, middle, and bottom. We were better able to comprehend how the behavior of the material varies from the bottom to the top of the part thanks to these testing. The average hardness values from the microhardness test were 221.35 HV for the bottom, 240.68 HV for the middle, and 212.55 HV for the top. The top of these figures is quite similar to the reference (-1.14% difference), the middle is much higher ($+11.95\%$), and the bottom is also slightly higher ($+2.96\%$) as compared to a standard reference value of 215 HV for regular (non-printed) SS316L. The heating and cooling that takes place during printing is the cause of this fluctuation. Because of the layers deposited above it, the central portion of the print is exposed to heat several times. The metal's structure may get stronger and finer as a result of the additional heating and gradual cooling, which raises the hardness. In contrast, the upper portion has a somewhat lower hardness since it cools off rapidly and is rarely reheated. The bottom portion has a harder texture than the other two since it was supported by the base plate and underwent mild reheating.

The sample's various internal stress types were revealed by the XRD data. Tensile tension was detected in the upper portion, indicating internal pulling. The bottom portion also experienced compressive stress, although not as much as the middle portion, which indicates that it being squeezed from the inside. The way the object cools down after each layer is printed is what causes these stress patterns. The layers below prevent the top from shrinking as it cools quickly, causing pulling (tensile) tension. As more layers are added, the center is heated and cooled numerous times, which leads to the accumulation of squeezing (compressive) stress. The bottom part, which stays close to the cooler base plate, also has compressive stress, but less than the middle.

The differences in stress and hardness from bottom to top are simply caused by the amount of heat that each section receives during printing. This demonstrates that cooling and temperature

have a significant impact on the finished printed metal's quality. Patterns like these are typical in LWDED and should be considered while designing parts with this technique.

In conclusion, this work demonstrated that LWDED may be utilized to create robust SS316L parts, but the properties vary across the part. Future efforts to create better and more dependable LWDED parts can benefit from these findings and testing techniques.

The research is concerned with the Laser Wire Direct Energy Deposition (LWDED) process and how it influences the material properties of SS316L stainless steel. The principal areas discussed in the research are:

1. **Material Analysis:** Experiments to study the microstructural features, such as grain size, porosity, and morphology, of the deposited SS316L layers with the help of Field Emission Scanning Electron Microscopy (FESEM).
2. **Measurement of Residual Stress:** Assessment of residual stresses in LWDED-processed material using X-Ray Diffraction (XRD) methods.
3. **Mechanical Testing:** Microhardness measurement in the deposited and heat-affected zones to determine the impact of the LWDED process on mechanical properties of SS316L.
4. **Process Optimization:** The research will determine the critical process parameters (laser power, scan speed, and layer thickness) that affect the final properties of the material.
5. The research is intended to make a contribution towards the knowledge of LWDED for stainless steel parts and assess its applicability in industrial processes where residual stress control, material integrity, and mechanical performance are paramount.

Future Scope:

1. **No Numerical Simulation:** The research does not involve numerical simulation of the development of residual stress or thermal behavior modeling during the LWDED process. Experimental techniques only (XRD, FESEM, microhardness) are utilized.
2. **Post-Processing Issues:** Even though post-processing treatments like heat treatment can affect residual stresses and mechanical properties, such effects can be studied in detail by this research.
3. **Range of Mechanical Tests:** The mechanical tests are constrained to microhardness measurements and do not go beyond to include thorough tests like tensile strength, fatigue, or fracture toughness, which would be required to assess material performance fully.

-
4. Environmental Factors: The experiment is performed under laboratory-controlled conditions, and the outcomes can differ in an industrial context at larger scales, especially in more variable or complex environmental conditions.

These limitations indicate the scope of the study and targeted focus on SS316L stainless steel in the context of the LWDED process. Further post-processing methods and extensive mechanical testing can yield further details regarding the long-term behaviour of LWDED components. The lack of numerical simulation in this research provides possibilities for future research in predictive modelling of residual stresses and thermal behaviour. Overall, the findings of this research will provide useful information for enhancing the additive manufacturing process and understanding SS316L material behaviour in LWDED.

REFERENCES

- [1] “ISO/ASTM 52900:2021(en), Additive manufacturing — General principles — Fundamentals and vocabulary.” Accessed: Apr. 30, 2025. [Online]. Available: <https://www.iso.org/obp/ui/#iso:std:iso-astm:52900:ed-2:v1:en>
- [2] K. P. Karunakaran, A. Bernard, S. Suryakumar, L. Dembinski, and G. Taillandier, “Rapid manufacturing of metallic objects,” *Rapid Prototyp. J.*, vol. 18, no. 4, pp. 264–280, Jun. 2012, doi: 10.1108/13552541211231644.
- [3] K. Reddy and S. Tolcha, “ADDITIVE MANUFACTURING TECHNOLOGIES,” Jul. 2019.
- [4] I. Gibson, D. Rosen, and B. Stucker, “Development of Additive Manufacturing Technology,” in *Additive Manufacturing Technologies: 3D Printing, Rapid Prototyping, and Direct Digital Manufacturing*, I. Gibson, D. Rosen, and B. Stucker, Eds., New York, NY: Springer, 2015, pp. 19–42. doi: 10.1007/978-1-4939-2113-3_2.
- [5] “What is Directed Energy Deposition (DED) 3D Printing? | Sciaky.” Accessed: May 21, 2025. [Online]. Available: <https://www.sciaky.com/additive-manufacturing/what-is-ded-3d-printing>
- [6] “Material Extrusion | Additive Manufacturing Research Group | Loughborough University.” Accessed: May 21, 2025. [Online]. Available: <https://www.lboro.ac.uk/research/amrg/about/the7categoriesofadditivemanufacturing/material-extrusion/>
- [7] S. Cooke, K. Ahmadi, S. Willerth, and R. Herring, “Metal additive manufacturing: Technology, metallurgy and modelling,” *J. Manuf. Process.*, vol. 57, pp. 978–1003, Sep. 2020, doi: 10.1016/j.jmapro.2020.07.025.
- [8] T. D. Ngo, A. Kashani, G. Imbalzano, K. T. Q. Nguyen, and D. Hui, “Additive manufacturing (3D printing): A review of materials, methods, applications and challenges,” *Compos. Part B Eng.*, vol. 143, pp. 172–196, Jun. 2018, doi: 10.1016/j.compositesb.2018.02.012.
- [9] F. M. Quaresma Ramalho, M. Alves, M. Correia, L. Vilhena, and A. Ramalho, “Study of Laser Metal Deposition (LMD) as a Manufacturing Technique in Automotive Industry,” 2020, pp. 225–239. doi: 10.1007/978-3-030-29041-2_29.
- [10] “Laser Metal Deposition - an overview | ScienceDirect Topics.” Accessed: May 01, 2025. [Online]. Available: <https://www.sciencedirect.com/topics/engineering/laser-metal-deposition>
- [11] F. Liu, S.-S. Ji, T. Shi, L. Wan, S.-H. Shi, and G.-Y. Fu, “Parametric study of the three-beam laser inside coaxial wire feeding additive manufacturing,” *Int. J. Adv. Manuf. Technol.*, vol. 123, no. 1, pp. 313–330, Nov. 2022, doi: 10.1007/s00170-022-10144-z.
- [12] M. Ghasempour-Mouziraji, J. Lagarinhos, D. Afonso, and R. Alves de Sousa, “A review study on metal powder materials and processing parameters in Laser Metal Deposition,” *Opt. Laser Technol.*, vol. 170, p. 110226, Mar. 2024, doi: 10.1016/j.optlastec.2023.110226.
- [13] S. Chen, H. Gao, Y. Zhang, Q. Wu, Z. Gao, and X. Zhou, “Review on residual stresses in metal additive manufacturing: formation mechanisms, parameter dependencies, prediction and control approaches,” *J. Mater. Res. Technol.*, vol. 17, pp. 2950–2974, Mar. 2022, doi: 10.1016/j.jmrt.2022.02.054.
- [14] Z. Zhang, “A Review on Modelling and Simulation of Laser Additive Manufacturing: Heat Transfer, Microstructure Evolutions and Mechanical Properties,” *coatings*, vol. 12, no. 9, Sep. 2022, doi: 10.3390/coatings12091277.

-
- [15] “Heat Source Modeling and Residual Stress Analysis for Metal Directed Energy Deposition Additive Manufacturing.” Accessed: May 01, 2025. [Online]. Available: <https://www.mdpi.com/1996-1944/15/7/2545>
- [16] A. J. Sterling, B. Torries, N. Shamsaei, S. M. Thompson, and D. W. Seely, “Fatigue behavior and failure mechanisms of direct laser deposited Ti–6Al–4V,” *Mater. Sci. Eng. A*, vol. 655, pp. 100–112, Feb. 2016, doi: 10.1016/j.msea.2015.12.026.
- [17] C. Verma, A. Alameri, I. Barsoum, and A. Alfantazi, “Review on corrosion-related aspects of metallic alloys additive manufactured with laser powder bed-fusion (LPBF) technology,” *Prog. Addit. Manuf.*, pp. 1–29, Sep. 2024, doi: 10.1007/s40964-024-00810-x.
- [18] M. R. Khosravani and T. Reinicke, “On the Use of X-ray Computed Tomography in Assessment of 3D-Printed Components,” *J. Nondestruct. Eval.*, vol. 39, no. 4, Dec. 2020, doi: 10.1007/s10921-020-00721-1.
- [19] M. E. Fitzpatrick, A. T. Fry, P. Holdway, F. A. Kandil, J. Shackleton, and L. Suominen, “Determination of residual stresses by X-ray diffraction.” Accessed: May 09, 2025. [Online]. Available: <https://eprintspublications.npl.co.uk/2391/>
- [20] M. Abuabiah *et al.*, “Advancements in Laser Wire-Feed Metal Additive Manufacturing: A Brief Review,” *Materials*, vol. 16, no. 5, Art. no. 5, Jan. 2023, doi: 10.3390/ma16052030.
- [21] M. Q. Zafar *et al.*, “A Review on Metal Additive Manufacturing - Types, Applications and Future Trends,” *Recent Prog. Mater.*, vol. 7, no. 1, Art. no. 1, Feb. 2025, doi: 10.21926/rpm.2501006.
- [22] J. A. D.-D. la Peña, P. A. Limon-Leyva, P. Cortes, and K. Choo, “Modeling of Direct Energy Deposition for Wire Laser Additive Manufacturing,” *J. Mater. Eng. Perform.*, Jan. 2025, doi: 10.1007/s11665-025-10665-0.
- [23] M. Taghizadeh and Z. H. Zhu, “A comprehensive review on metal laser additive manufacturing in space: Modeling and perspectives,” *Acta Astronaut.*, vol. 222, pp. 403–421, Sep. 2024, doi: 10.1016/j.actaastro.2024.06.027.
- [24] F. Guagliione, A. A. Benni, and B. Previtali, “Exploring wire laser metal deposition of 316L stainless steel as a viable solution for combined manufacturing routes,” *Prog. Addit. Manuf.*, Nov. 2024, doi: 10.1007/s40964-024-00832-5.
- [25] N. Brubaker *et al.*, “Investigating Microstructure and Properties of 316L Stainless Steel Produced by Wire-Fed Laser Metal Deposition,” *J. Mater. Eng. Perform.*, vol. 31, no. 5, pp. 3508–3519, May 2022, doi: 10.1007/s11665-021-06477-7.
- [26] A. Kiran, Y. Li, J. Hodek, M. Brázda, M. Urbánek, and J. Džugan, “Heat Source Modeling and Residual Stress Analysis for Metal Directed Energy Deposition Additive Manufacturing,” *Materials*, vol. 15, no. 7, Art. no. 7, Jan. 2022, doi: 10.3390/ma15072545.
- [27] J. Wang *et al.*, “Failure Analysis of a Chromium Plating Layer on a Piston Rod Surface and the Study of Ni-Based Composite Coating with Nb Addition by Laser Cladding,” *Metals*, vol. 12, p. 1194, Jul. 2022, doi: 10.3390/met12071194.
- [28] Y. Zhang, W. Yu, Z. Zheng, and Y. Lai, “A comprehensive review of residual stress in metal additive manufacturing: detection techniques, numerical simulation, and mitigation strategies,” *J. Braz. Soc. Mech. Sci. Eng.*, vol. 47, no. 1, p. 17, Dec. 2024, doi: 10.1007/s40430-024-05319-6.
- [29] A. Madariaga, G. Ortiz-de-Zarate, and P. J. Arrazola, “Non-destructive procedure to determine residual stresses and white layers in hole making operations,” *NDT E Int.*, vol. 151, p. 103304, Apr. 2025, doi: 10.1016/j.ndteint.2024.103304.
- [30] I. C. Noyan and J. B. Cohen, *Residual Stress*. New York, NY: Springer, 1987. doi: 10.1007/978-1-4613-9570-6.

-
- [31] A. Kumar, R. Mahanti, and M. Das, "Investigation of electropolishing performance on surface residual stress and morphology of electrical discharge machined maraging steel." Accessed: May 23, 2025. [Online]. Available: <https://journals.sagepub.com/doi/full/10.1177/09544062221140735#disp-formula5-09544062221140735>
- [32] "Meltio M450 - Metal 3D Printer | Meltio." Accessed: May 01, 2025. [Online]. Available: <https://meltio3d.com/metal-3d-printers/meltio-m450/>
- [33] M. A. Belsvik, W. M. Tucho, and V. Hansen, "Microstructural studies of direct-laser-deposited stainless steel 316L-Si on 316L base material," *SN Appl. Sci.*, vol. 2, no. 12, p. 1967, Nov. 2020, doi: 10.1007/s42452-020-03530-3.